High-resolution three-dimensional azimuthal velocity anisotropy of S-waves in southern-central Japan, based on ambient noise tomography

Bokani Nthaba[1,2], Tatsunori Ikeda[1,3], Takeshi Tsuji[1,3,4*] and Yoshihisa Iio[5]

Abstract

To investigate the dominant deformational patterns and stress conditions in the upper crustal structure of the Kinki region, southern-central Japan, we constructed a high-resolution 3D azimuthal anisotropy model to a depth of ~11 km. We used 6-month-long ambient noise data recorded by the densely distributed permanent and temporary stations. From this dataset, cross-correlations were retrieved. We then obtained a 3D isotropic velocity model by inverting Rayleigh wave dispersion data, followed by a direct joint inversion for both 3D azimuthal anisotropy and additional isotropic velocity perturbation. The resolved 3D azimuthal anisotropy reveals significant contrasts of anisotropy across the Kinki region. The predominant fast axes observed in the northwestern Kinki region align with the direction of the maximum horizontal compressional stress and the principal strain rate axes, suggesting that the observed anisotropy is mainly stress-induced. In the southern part of the study area, furthermore, the predominant fast axes trend NE–SW and near E–W, also indicating the presence of stress-induced anisotropy. On the depth profile of the anisotropy, we found depth-dependent variation of azimuthal anisotropy. There exists a significant consistency between the anisotropy observed beneath 3 km depth and the dense distribution of earthquake hypocenters. This interrelationship between anisotropy and seismicity demonstrates that the observed anisotropy could be linked to local crustal stress or fractures relevant to earthquake ruptures. Our 3D anisotropy model therefore contributes towards understanding the locations and features of the seismicity region.

Keywords Azimuthal anisotropy, Ambient noise tomography, S-wave velocity, Surface waves, Crustal stress, Fracture
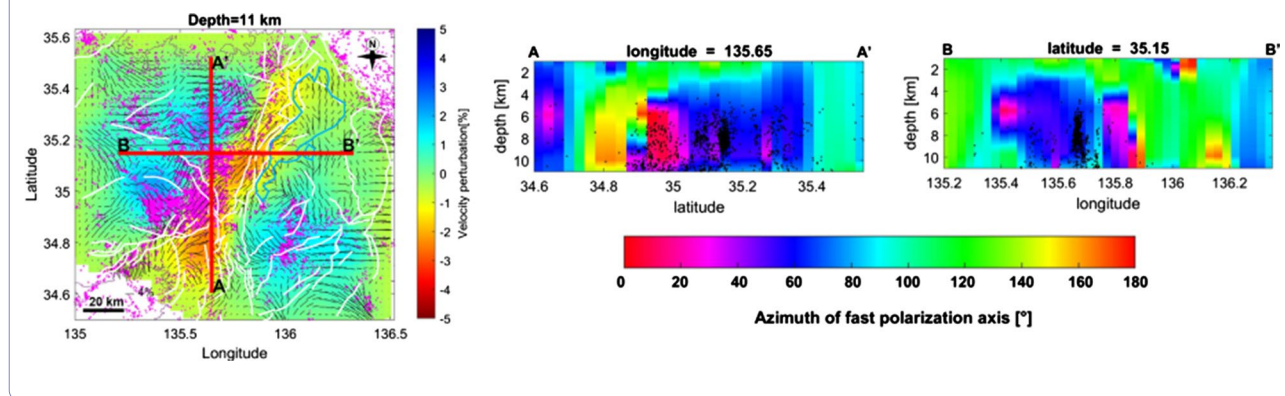
*Correspondence:
Takeshi Tsuji
tsuji@sys.t.u-tokyo.ac.jp
Full list of author information is available at the end of the article

Nthaba *et al. Earth, Planets and Space* (2023) 75:102

Page 2 of 21

Graphical Abstract

Introduction

Geological heterogeneities can be well constrained by isotropic seismic velocities obtained from high-resolution seismic tomographic inversions (e.g., Nakajima and Hasegawa 2007; Nishida et al. 2008; Nthaba et al. 2022; Matsubara et al. 2008; Suemoto et al. 2020). However, the geodynamic processes that cause deformation and generate destructive earthquakes can be revealed by a seismically observable phenomena referred to as anisotropy (Chen et al. 2018; Hiramatsu et al. 2010; Teanby et al. 2004), which reflects the directional variation of seismic velocity (Bem et al. 2022). Anisotropic structure is caused by the shape-preferred orientation (SPO) or lattice-preferred orientation (LPO) of anisotropic minerals (Crampin and Peacock 2008; Savage 1999; Wang and Zhao 2021), as well as the fault fabrics or shearing in fault systems in the upper crust (Balfour et al. 2005; Boness and Zoback 2006). Although seismic anisotropy sources in the crust are often difficult to identify due to the structural complexity of the crust (Balfour et al. 2005), numerous studies have demonstrated that the seismic anisotropy in the crust is mainly attributable to the existence of fluid-filled microcracks aligned parallel to the maximum axis of applied stress (Chang et al. 2015; Crampin 1998; Crampin and Peacock 2008; Legendre et al. 2021; Mizuno et al. 2001; Yang et al. 2018). Proximal to major strike-slip faults, seismic anisotropy measurements reveal that frictionally weak faults are likely to have local influence on seismic anisotropy (Balfour et al. 2005; Boness and Zoback 2006).

Seismic anisotropy in the crust and upper mantle has been widely studied using different seismological methods (e.g., Chen et al. 2018; Crampin 1977; Li et al. 2019; Liu C et al. 2019; Tsuji et al. 2011a; Wang et al. 2016; Wu et al. 2021; Xu et al. 2021). In this study, we focus on the azimuthal anisotropy of S-waves in the Kinki region, southern-central Japan, which is an area with complex geologic heterogeneities and rich tectonic history (Fig. 1). Moreover, the prevailing crustal movement as manifested in active faulting and shallow earthquake occurrences make the Kinki region an ideal natural laboratory for the study of fundamental deformational mechanisms and patterns. The azimuthal anisotropy in the Kinki region has been studied in the northern part (Inner Zone) by shear-wave splitting of natural earthquake (Hiramatsu et al. 2010; Kaneshima et al. 1987; Mizuno et al. 2001). These studies revealed some consistency between anisotropy and the axis of maximum horizontal compression stress (Ando 1979), suggesting that anisotropy in the northern part of the Kinki region is predominantly stress-induced, rather than structure-induced. However, it should be noted that the depth of anisotropy that causes shear waves to split is poorly resolved because the observed shear-wave splitting represents a combined effect of seismic anisotropy along long raypaths (Guo and Chen 2017; Savage 1999; Wang and Zhao 2021). Hence, the variation of azimuthal anisotropy with depth remains unknown in the Kinki region. Furthermore, the sparse distribution of seismic events and stations used by the previous studies prevents the mapping of lateral heterogeneities of the anisotropic regions at a high spatial resolution. Therefore, it has been difficult to resolve the anisotropic features related to the localized faults.

In this study, we exploit the availability continuously recorded seismic ambient noise data from the dense seismic network deployed in the Kinki region (Iio et al. 2018; Katoh et al. 2018) to construct a high-resolution 3D azimuthal anisotropy model (Fig. 1). Compared with
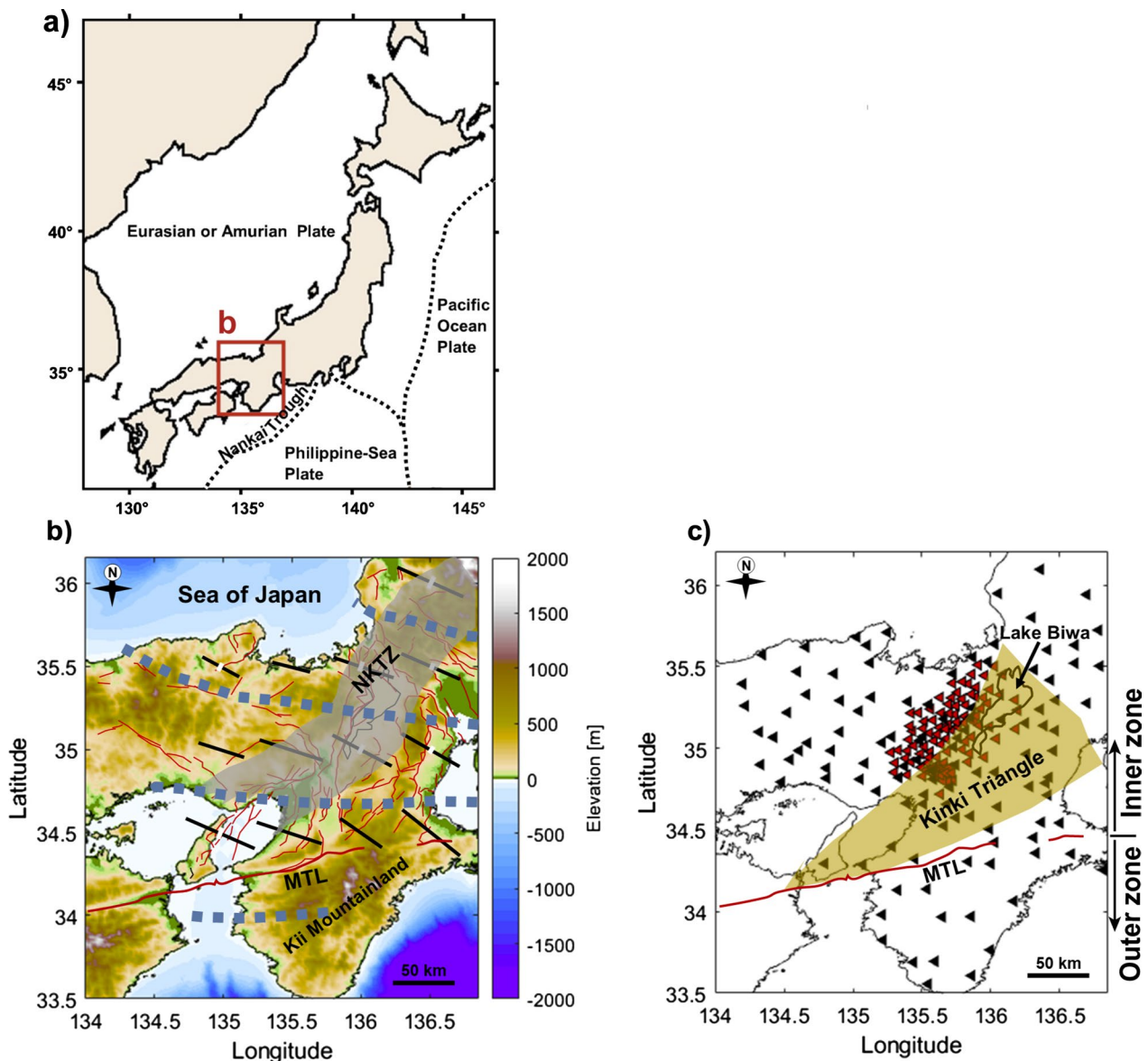
Fig. 1 **a** Map showing the location of the Kinki region within the islands of Japan. **b** Topographic map of the Kinki region. Black and white bars show the principal strain rate axes (black bars: compression, white bars: extension) (Sagiya et al. 2000). Blue dashed lines indicate the compressional stress trajectories (Ukawa 1982). **c** The distribution of permanent (black triangles) and temporary stations (red triangles) deployed in the Kinki region. Red lines in **b** represent active faults (Research Group for Active Faults of Japan 1991), thick, gray-shaded line shows the inferred location of the Niigata-Kobe Tectonic Zone (NKTZ). Also shown here is the location of the Median Tectonic Line (MTL)

the shear-wave splitting based on natural earthquake, we estimate high spatial resolution azimuthal anisotropy using a surface wave tomography approach of Liu et al. (2019a), which is well suited to constraining depth-varying deformation patterns in the crust (Adimah and Padhy 2020; Chen et al. 2015, 2018; Liu et al. 2019a; Ojo et al. 2018). Our results could provide further constraints on the geodynamic processes of crustal deformation in the entire Kinki region.

Geologic setting

Central Japan is a complex region subject to the subduction of the Philippine Sea Plate (PSP) beneath the Eurasian or Amurian (Amur) plate, as well as to stress from the Pacific Oceanic Plate (Fig. 1; Barnes 2008). Moreover, a shift in the direction and rate of subduction of the PSP and eastward movement of the incipient Amur Plate is postulated to have initiated a change in compression direction from N–S to E–W, marking the beginning

Nthaba *et al. Earth, Planets and Space*   (2023) 75:102

Page 4 of 21

of a new (neo) tectonic regime for the Japanese islands (Barnes 2008). These processes have engendered relatively new, large fault systems and continually reactivates the old ones. In the Kinki region, southern-central Japan, a striking example of neotectonic faulting is the right-lateral strike-slip Median Tectonic Line (MTL), which trends E–W across the Kii Peninsula (Fig. 1b). The MTL divides the Kinki region into two zones with different characteristics and deformational styles (Okamura and Shishikura 2020; Sato et al. 2015); the Inner Zone (northern part) and the Outer Zone (southern part) (Fig. 1c).

The Outer Zone is characterized by undulating topographic pattern of mountainous and depressional zones, and active faults are scarce (Okamura and Shishikura 2020). Right-lateral sense of motion on the MTL is active to the west of the Kii Mountainland, and is dormant to the east (Nakata and Imaizumi 2002). In contrast, crustal deformation in the Inner Zone shows that the crust is being compressed in a E–W to ESE–WNW direction (Barnes 2008; Choi et al. 2011; Okamura and Shishikura 2020). Elongated NE–SW to ENE–WSW trending sedimentary basins developed in Pliocene time, and the Inner Zone has been deformed during Quaternary by numerous active faults that engendered tectonic ridges and altered the basins (Huzita 1980; Sugiyama 1992). These Quaternary active faults include conspicuous reverse faults predominantly trending N–S, and NE–SW and NW–SE oriented strike-slip faults prevalent in the Kinki Triangle (shaded area in Fig. 1c; Huzita 1980), produced by the E–W to ESE–WNW compressional stress (Okamura and Shishikura 2020).

Furthermore, Sagiya et al. (2000) identified a NE–SW-trending zone of high strain rate across the Kinki region, designated the Niigata-Kobe Tectonic Zone (NKTZ). The NKTZ, just like the Kinki Triangle (Fig. 1c), hosts NE–SW-striking Quaternary fault zones which are oriented in the same direction as the NKTZ (Tamura et al. 2020) and many destructive earthquakes have occurred in this zone.

Data and methods
We used the vertical component of the continuous seismic waveforms recorded in the year 2019 from April 1–September 30 by a total of 114 permanent stations (black triangles in Fig. 1c) and 104 temporary stations (red triangles in Fig. 1c). The detailed information on these seismometers was described in Nthaba et al. (2022). With these permanent and temporary stations, we obtained a dataset with adequate ray paths coverage of short-period surface waves, which enabled us to construct high-resolution models of 3D S-wave velocity (V_{SV}) azimuthal anisotropy and isotropic V_{SV} perturbations.

Dispersion curves between station pairs
Detailed description of the processing routine and the methods adopted to estimate dispersion curves between station pairs used for this study is given in our earlier paper (Nthaba et al. 2022). Here, we briefly describe the steps followed to avoid repetition. The daily seismic records were partitioned into 30-min-long segments with a 50% overlap before removing the instrumental response. We then computed the cross-correlation spectra from the resulting seismograms for all the station pairs (Ekström 2014). Then, we stacked the daily cross-correlation spectra over a period of 6 months. After obtaining the stacked cross-correlations, we used the GSpecDisp package (Sadeghisorkhani et al. 2018) to uniquely measure the phase velocity dispersion curves by the zero-crossing method (Ekström et al. 2009) in the period range from 1 s to a maximum of 20 s. Within this period range, we used a signal-to-noise ratio (SNR) of 10 as a threshold to reject cross-correlations with low signal. Here we defined the SNR as the ratio between maximum absolute amplitude in the signal window (between arrival times corresponding to waves with 1 and 4.5 km/s) and the root mean square amplitude in the noise time window (between 500 and 700 s). Using this SNR criterion, we obtained a total of 23,647 dispersion curves for the inversion.

S-wave azimuthal anisotropy by a direct inversion technique
We estimated the 3D azimuthally anisotropic Vsv structure from phase velocity dispersion data by applying a direct joint inversion technique proposed by Liu et al. (2019a), abbreviated DAzimSurfTomo. For the conventional two-step anisotropic inversion approaches (Montagner and Nataf 1986; Montagner and Tanimoto 1991; Yao et al. 2010), the initial step of phase velocity tomography involves estimating the isotropic and azimuthally anisotropic phase velocity variations by utilizing mixed-path dispersion data. In the second step, the depth-dependent S-wave velocity and its azimuthal anisotropy can be obtained by inverting the pointwise dispersion curve with azimuthal anisotropy (Liu et al. 2019a). By contrast, this direct joint inversion approach circumvents the intermediate step of constructing 2D phase velocity azimuthal anisotropy maps. Additionally, it accounts for the frequency-dependent ray-bending effect using the fast-marching method (Rawlinson and Sambridge 2004) in estimation of frequency-dependent Rayleigh wave propagation in the first step of isotropic inversion (Fang et al. 2015; Li et al. 2016), and the second step of joint inversion, where the effect of weak azimuthal anisotropy on the raypaths is ignored (Liu et al. 2019a). Accounting for the ray-bending effects in the inversion makes this approach

Nthaba *et al. Earth, Planets and Space* (2023) 75:102

Page 5 of 21

valid for complex heterogeneous media (Yang and Hung 2005).

The raypath of Rayleigh waves between source A and receiver B may detour from the great-circle path due to structural heterogeneity (Liu et al. 2019a). Taking the variation of azimuthal anisotropy ψ into account, the travel time between A and B $t_{AB}(\omega)$ based on ray theory can be expressed as:

$$t_{AB}(\omega) = \int_{l_{AB}} \frac{1}{c(l, \omega, \psi)} dl, \tag{1}$$

where $c(l, \omega, \psi)$ represents the local phase velocity along the actual raypath l_{AB}, ω is the angular frequency and ψ indicates the azimuth of Rayleigh wave propagation. The discretized version of Eq. (1) is given as:

$$t_{AB}(\omega) = \sum_{p=1}^{P} \frac{1}{c_p(\omega, \psi)} \Delta l, \tag{2}$$

where P is the total number of path segments, p is the index of path segments, and $c_p(\omega, \psi)$ represents the phase velocity for the path segment Δl along raypath AB. For a weak anisotropic medium, the Rayleigh wave phase velocity $c(\omega, \psi)$ in Eq. (2) can be expressed as (Smith and Dahlen 1973):

$$c_p(\omega, \psi) = c_0(\omega, p) + a_1(\omega, p)cos2\psi + a_2(\omega, p)sin2\psi + a_3(\omega, p)cos4\psi + a_4(\omega, p)sin4\psi, \tag{3}$$

where $c_0(\omega)$ represents the isotropic phase velocity at the angular frequency ω, and $a_{1,2}$ and $a_{3,4}$ are the amplitudes of 2ψ (180° periodicity) and 4ψ (90° periodicity) terms, respectively. As suggested in Montagner and Nataf (1986), the 4ψ terms in Eq. (3) are insignificant for Rayleigh waves.

Due to the variations in effective transversely isotropic moduli (ETI) and azimuthally anisotropic moduli (AA) relative to the reference moduli, phase velocity perturbation (Eq. 3) can be decomposed into three parts:

$$c(\omega, \psi) = c_0^{ref}(\omega) + \delta c_k^{ETI}(\omega) + \delta c_k^{AA}(\omega, \psi), \tag{4}$$

where $c_0^{ref}(\omega)$ is the prediction from reference moduli. The study area is parameterized with a regular grid of K points in total. The 1D transversely layered model at each grid point k is then taken as a reference with the isotropic phase velocity given by c_0^k. For a tomographic model, the objective is to minimize the traveltime difference between the measured traveltimes $t_i^{obs}(\omega)$ and the calculated traveltimes from the model for all frequencies ω. With the isotropic phase velocity $c_0^k(\omega)$ as a reference, the traveltime difference between the measurement $t_i^{obs}(\omega)$ and the isotropic reference model prediction $t_i^{ref}(\omega)$ can be expressed as:

$$\delta t_i(\omega) = t_i^{obs}(\omega) - t_i^{ref}(\omega) \approx \sum_{k=1}^{K} \frac{R_k}{\left(c_0^k(\omega)\right)^2}$$
$$\left(\delta c_k(\omega) + a_1^k(\omega)cos2\psi + a_2^k(\omega)sin2\psi\right)$$
$$= \sum_{k=1}^{K} \frac{R_k}{\left(c_0^k(\omega)\right)^2} \left(\delta c_k^{ETI}(\omega) + \delta c_k^{AA}(\omega, \psi)\right), \tag{5}$$

where R_k is the coefficient of interpolation.

Following Liu et al. (2019a), the effective transversely isotropic perturbation of Rayleigh wave phase velocity can be expressed as:

$$\delta c_k^{ETI}(\omega) = \int_0^{\infty} \left(\frac{\partial c_k(\omega)}{\partial A_k(z)} \delta A_k(z) + \frac{\partial c_k(\omega)}{\partial C_k(z)} \delta C_k(z) + \frac{\partial c_k(\omega)}{\partial L_k(z)} \delta L_k(z) + \frac{\partial c_k(\omega)}{\partial F_k(z)} \delta F_k(z) \right) dz, \tag{6}$$

where the four parameters A, C, L, and F together with another, N, represent parameters of the transversely isotropic medium. According to Montagner and Nataf (1986), the azimuthally anisotropic perturbation in the Rayleigh wave phase velocities can be approximated by:

$$\delta c_k^{AA}(\omega, \psi) \approx \int_0^{\infty} \left[\left(B_c^k \frac{\partial c_k(\omega)}{\partial A_k(z)} + G_c^k \frac{\partial c_k(\omega)}{\partial L_k(z)} \right)cos2\psi + \left(B_s^k \frac{\partial c_k(\omega)}{\partial A_k(z)} + G_s^k \frac{\partial c_k(\omega)}{\partial L_k(z)} \right)sin2\psi \right] dz, \tag{7}$$

where B_c, B_s, G_c, and G_s represent the 2ψ azimuthal variations of A and L, respectively (Liu et al. 2019a; Montagner and Nataf 1986). Equationa (6) and (7) can then be substituted into Eq. (5) to obtain the traveltime perturbation at all frequencies $\delta t_i(\omega)$ (Liu et al. 2019a). $\delta t_i(\omega)$ can be expressed in the classical inversion function as:

$$\mathbf{d} = \mathbf{Gm}, \tag{8}$$

where $\mathbf{d}$ represents the vector of the traveltime residuals for all frequencies and all paths, $\mathbf{G}$ is the data sensitivity matrix. The model parameter vector $\mathbf{m}$ is expressed as:

$$\boldsymbol{m} = \left[\delta\beta_1(z_1) \ldots \delta\beta_1(z_J) \ldots \delta\beta_K(z_J) \frac{G_c^1(z_1)}{L_1(z_1)} \ldots \frac{G_c^1(z_J)}{L_1(z_J)} \ldots \frac{G_c^K(z_J)}{L_K(z_J)} \frac{G_s^1(z_1)}{L_1(z_1)} \ldots \frac{G_s^1(z_J)}{L_1(z_J)} \ldots \frac{G_s^K(z_J)}{L_K(z_J)} \right]^T. \tag{9}$$

Nthaba *et al. Earth, Planets and Space* (2023) 75:102

Page 6 of 21

Equation (8) is then solved by the LSQR algorithm (Paige and Saunders 1982) with the regularized inversion system:

$$
\begin{bmatrix} \boldsymbol{G}_{iso} & \boldsymbol{G}_{AA} \\ \lambda_1 \boldsymbol{L}_{iso} & 0 \\ 0 & \lambda_2 \boldsymbol{L}_{AA} \end{bmatrix} \begin{bmatrix} \boldsymbol{m}_{iso} \\ \boldsymbol{m}_{AA} \end{bmatrix} = \begin{bmatrix} \boldsymbol{d} \\ 0 \\ 0 \end{bmatrix},
\tag{10}
$$

where $\boldsymbol{G}_{iso}$, $\boldsymbol{G}_{AA}$, $\boldsymbol{m}_{iso}$, and $\boldsymbol{m}_{AA}$ represent the isotropic and azimuthal anisotropic data sensitivity matrices and model parameter vectors, respectively, $\boldsymbol{L}_{iso}$ and $\boldsymbol{L}_{AA}$ are the isotropic and azimuthally anisotropic roughening matrices, and λ_1 and λ_2 are the weighting parameters balancing data fitting and model regularization. Since the isotropic *Vsv* model is iteratively updated, new depth-dependent sensitivity kernel matrices and new raypaths for all isotropic and anisotropic parameters are also updated in each iteration. The inversion workflow using the DAzimSurfTomo method is implemented in two stages. Firstly, the 3D isotropic *Vsv* model is obtained by inverting Rayleigh wave phase velocities using a 3D direct inversion method (Fang et al. 2015). Then, the isotropic *Vsv* model obtained from the first step is used as the 3D reference model to perform a joint inversion iteratively for both 3D isotropic *Vsv* perturbation and azimuthal anisotropy. According to Liu et al. (2019a), the azimuthal anisotropic S-wave velocity $\widehat{V}_{SV}$ can be approximated by:

$$
\begin{aligned}
\widehat{V}_{SV} &\approx V_{SV}\left(1 + \frac{G_c}{2L}cos2\psi + \frac{G_s}{2L}sin2\psi\right) \\
&= V_{SV}[1 + A_{SV}cos2(\psi - \varnothing)],
\end{aligned}
\tag{11}
$$

where V_{SV} represents the isotropic part of $\widehat{V}_{SV}$, A_{SV} is the magnitude of azimuthal anisotropy, $\varnothing$ represents the azimuth of fast polarization axis, which ranges from 0° to 180° clockwise from the north (Chen et al. 2015). A_{SV} and $\varnothing$ can be represented as:

$$
A_{SV} = \frac{1}{2}\sqrt{\left(\frac{G_s}{L}\right)^2 + \left(\frac{G_c}{L}\right)^2},
\tag{12}
$$

$$
\varnothing = \frac{1}{2}tan^{-1}\left(\frac{G_s}{G_c}\right).
\tag{13}
$$

We conducted two separate inversions in this study. Firstly, we performed the inversion for the Kinki region in its entirety. Here, we parameterized the inversion area into 55 by 60 grid points with lateral grid interval of 0.05° and set 6 grid points at variable intervals along the depth direction (0, 1, 3, 6, 10, and 16 km). The second inversion area is the central part of the Kinki region, where seismic stations are densely distributed (Fig. 1c). We parameterized this area into 42 by 57 grid points with lateral grid

point intervals of 0.03° and 8 grid points along the vertical direction (0.0, 0.6, 1.8, 3.5, 6.0, 10.0, 15.0, and 20.0 km). The weighting parameters balancing data fitting λ_1 and model regularization λ_2 were set to be 100 and 3, respectively, based on a trial-and-error basis. The magnitude of anisotropy is affected by the regularization parameter λ_2 (Liu et al. 2019a); it increases with an decrease in λ_2, and vice versa. For both inversions, we used dispersion data within a frequency range of 0.0714–1.0 Hz. To account for the influence of topography on our isotropic Vsv and azimuthal anisotropic models, we subtracted altitude value from the depth value at each grid point. Elevation values were smoothed by applying a moving 2D average smoothing filter with a window size of 18 km by 18 km before correcting for topographic effects.

Using the zero-crossing method to estimate dispersion data is based on the assumption of the uniform distribution of ambient noise sources. However, in practice, ambient noise sources are not homogeneously distributed (Takagi et al. 2018), which may result in inaccurate phase velocity estimations. Despite this, cross-correlation functions derived from the 6 months data exhibit good symmetry in the arrival time of causal and anti-causal parts (see Fig. 2b in Nthaba et al. 2022). Therefore, it could be possible to conduct anisotropy analysis using the estimated dispersion data.

Results

Resolution tests

To assess our dataset capacity for resolving isotropic and anisotropic structures and to demonstrate the quality of raypaths coverage (Fig. 2) beneath the seismic network deployed in the Kinki region, we conducted a checkerboard resolution test (Figs. 3, 4, 5). Synthetic input models composed of alterning high and low velocity anomalies and fast polarization axes oriented north–south and east–west. The anomaly size for both the 3D isotropic Vsv and anisotropic models was set to be ∼0.5° (∼55 km; Fig. 3a, b) and ∼0.21° (∼23.1 km; Fig. 4a, b). The isotropic velocity perturbation is ±4%, and the anisotropic anomalies with magnitudes of 5% and 4% are assumed for the entire Kinki region and the central part of the Kinki region, respectively, with orthogonal orientations assigned to adjacent cells (Figs. 3b and 4b). By applying the inversion workflow described in the last section using the synthetic isotropic and azimuthal anisotropy data, we obtained both the 3D isotropic Vsv perturbation and azimuthal anisotropy models.

The checkerboard resolution test reveal that isotropic anomalies of the size 0.21° (Fig. 4) in both longitude and latitude directions can be recovered sufficiently in the
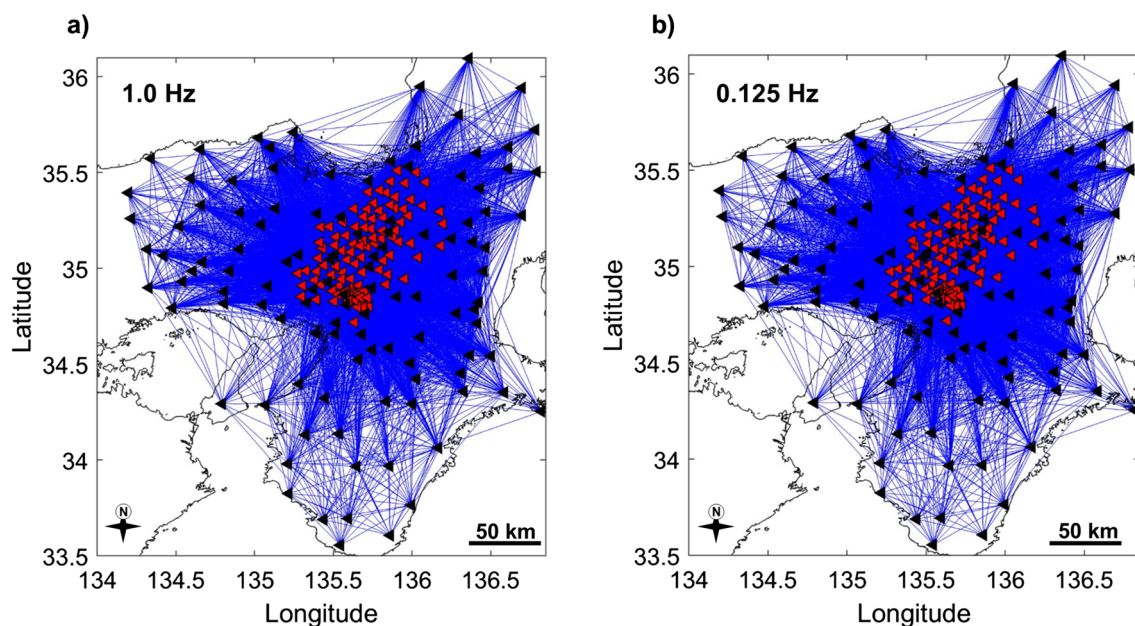
Fig. 2 Raypaths coverage derived from the inversion model at four frequencies: **a** 1.0 Hz, **b** 0.125 Hz. Black and red triangles represent the locations of permanent and temporary seismic stations, respectively. Blue lines represent the ray paths

central part of the study area where dense temporary stations are deployed, demonstrating that the density of ray path coverage is sufficient in this area. However, even isotropic anomalies of the size of about 0.5° (~ 55 km) laterally are poorly resolved on the edges of the Kinki region (Fig. 3). The poor resolution on the edges and the southern part of the Kinki region can be mainly attributable to sparsely distributed seismic stations in those areas. For anisotropic anomalies (Fig. 3d, f), anisotropy magnitude of about 4% and the orientations of the fast polarization axes could be sufficiently recovered beneath the densely distributed temporary stations. However, the strength of anisotropy is significantly weaker in areas with poor ray-path coverage, and the fast axes orientations deviate from the input on the edges and the southern end of the study area, where the raypaths coverage is insufficient.

In addition to the evaluation of horizontal resolution (Figs. 3 and 4), we performed a simple vertical resolution test to assess the variation of azimuthal anisotropy fast polarization axes for depth direction (Fig. 5). The input model for this test (Fig. 5a) comprises two layers with a 4% magnitude of anisotropy. The shallower layer has a

fast polarization axis oriented N–S, while the underlying layer has a fast polarization axis oriented E–W. We used the same inversion approach for this two layers model as the chckerboard resolution test for the horizontal direction (Figs. 3 and 4). The results of the vertical resolution test (Fig. 5) demonstrate that the anisotropy can be resolved although the results show small-scale fluctuations. Therefore, it could be difficult to interpret the small-scale (local) anomalies in the anisotropy results on depth profiles shown later.

Spatial distribution of isotropic and anisotropic velocities

The final isotropic S-wave velocity and azimuthal anisotropic models for the upper crustal structure of the Kinki region are illustrated in 3D horizontal slices (Figs. 6 and 7). The spatial distribution of the isotropic S-wave velocities is generally identical to our previous 3D S-wave velocity model (Nthaba et al. 2022) obtained using the same ambient noise data. Figure 6 represents the upper crustal structure of our whole study area with a depth range of 2 to 11 km. Figure 7, showing the upper crustal

(See figure on next page.)
Fig. 3 Checkerboard resolution test for the entire Kinki region. Input models: **a** 0.5° by 0.5° horizontal anomaly sizes of the isotropic velocity model, **b** anisotropic model of anomaly size 0.5° by 0.5° and fast polarization axes that are oriented perpendicular to each other (north and east). **c** and **e** Show the recovered velocity model (in **a**) at 3.5 and 6 km depth slices, respectively. The color bar (in percent) represents the isotropic velocity perturbation with respect to the reference velocity model, **d** and **f** show the recovered anisotropic model (in **b**) at 3.5 and 6 km depth levels, respectively
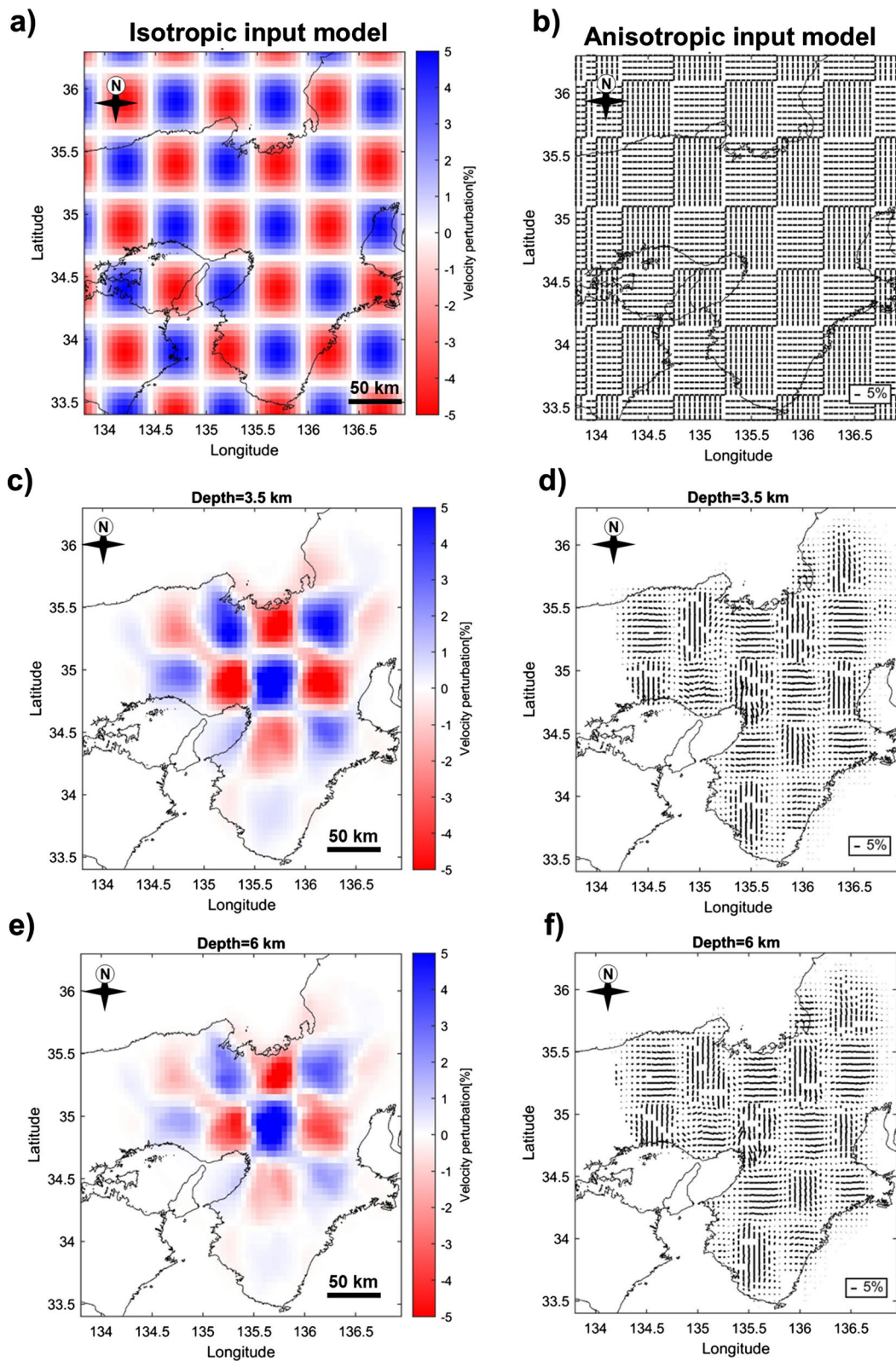
Fig. 3 (See legend on previous page.)

structure with a depth range of 1–11 km, represents the inverted results of the central part of the Kinki region.

The isotropic S-wave velocities are relatively higher on both sides of the NE–SW-trending low velocity zone (NKTZ) and of sedimentary basins (e.g., Osaka basin and Ise basin in Fig. 6b). The high velocity anomalies (A1, A2 and B in Fig. 6d) are spatially consistent with the location of mountain ranges, sedimentary complexes and intrusive rocks. Some of the low-velocity anomalies observed on the edges of the study area are not considered for discussion due to the lack of or minimal ray paths coverage in those areas. To assess the influence of isotropic velocity anomalies upon the estimated azimuthal anisotropy, we conducted an anisotropy recovery test (Fig. 8; Liu et al. 2019a). For this evaluation, to generate the synthetic data, we used the isotropic S-wave velocity model obtained from the first step (direct inversion) as the initial model, which did not contain any anisotropy. We then performed an inversion for anisotropy estimation. The results (Fig. 8) show a negligible magnitude of azimuthal anisotropy, demonstrating the robustness of the inversion method for anisotropy analysis.

We overlay the isotropic velocity perturbations with fast polarization axes of seismic anisotropy. Our results (Figs. 6 and 7) reveal significant lateral variations and complex patterns of azimuthal anisotropy across the Kinki region. The patterns of the observed azimuthal anisotropy change around the boundary between the Inner Zone and Outer Zone (i.e., MTL; Fig. 1c). In the Outer Zone, we observe azimuthal anisotropy with predominantly NE–SW and E–W or ENE–WSW fast axes directions. The E–W or ENE–WSW oriented fast axes can be observed in the western side of the Kii Mountainland (blue arrow in Fig. 6a), restricted within the low velocity zone and appear to be parallel to the MTL, whereas the NE–SW-oriented fast axes occur largely in the Kii Mountainland (red arrow in Fig. 6a) and are aligned in the same direction as the NE–SW-trending part of the high velocity feature (elevated zone; Fig. 1b).

Figure 7 represents the isotropic S-wave velocity and azimuthal anisotropic model of the central part of the Kinki region (part of the Inner Zone). Here, we identify three interesting anisotropy patterns. On the northwestern part of the Kinki region (undemarcated zone in Fig. 7), the fast axes directions are predominantly oriented E–W on the western portion of the high velocity

zone (A2 in Fig. 6d), and rotate to NW–SE towards the Sea of Japan. The pattern of anisotropy seems to be more complex in the shallow layer (Fig. 6a) than the observed ones in the underlying layers. Figure 6b–d (3–7 km depth slices) exhibits a concave up (NW–SE and NE–SW converging fast directions) anisotropy pattern. The strength of anisotropy within the upper layers (2–7 km; Fig. 6a–d) is relatively stronger than that within the deeper layers (9–11 km).

Beneath the north central area (a zone demarcated by dashed, magenta closed curves in Fig. 7), there exists significant depth-dependent variation of the fast direction axes. Within the upper layers (shallower than 3 km), the fast polarization axes are predominantly aligned in the NW–SE or nearly E–W (Fig. 7a). The direction of the fast axes changes to largely NE–SW in layers occurring from a depth range of 3–11 km, almost perpendicular to the NW–SE fast axes direction observed in the upper layers (less than 3 km). At 3 km depth (Fig. 7b), the NE–SW fast axis direction is consistent with the orientation of the high strain rate deformation zone, the NKTZ. We also note that from a depth of 3 km, these NE–SW-trending fast axes occur mainly within the eastern portion of the high velocity zones (A1 and A2 in Fig. 6d), then gradually spreads to the east towards the NE–SW-trending low velocity zone as the depth increases. The patterns of anisotropy within and around the high velocity zone denoted A2 in Fig. 6d significantly vary with depth. Furthermore, the magnitude of anisotropy in this area is stronger than in other parts of the study area (exceeding 4%).

The northeastern part of the study area (a zone demarcated by dashed, black closed curves in Fig. 7) forms part of the Kinki Triangle (Fig. 1c). It is characterized by significant lateral variations of the fast axes directions. Converging NW–SE and NE–SW fast axes directions and some curvilinear patterns are evident in this area. Slightly to the north of the MTL (high velocity zone denoted B in Fig. 6d), the observed fast axes are largely oriented NW–SE. The magnitude of anisotropy here is much stronger between 3 and 9 km depth slices (Fig. 7b–f) in the high velocity zone (∼4%), where the fast polarization axes are predominantly aligned in the NW–SE direction (Fig. 7).

In this study, we assumed a uniformly distributed noise source. If the dominant noise sources are heterogeneous or limited, the estimated anisotropy could include errors.

(See figure on next page.)
Fig. 4 Checkerboard resolution test results for the central part of the Kinki region (Fig. 1c): **a** 0.21° by 0.21° horizontal anomaly sizes of the isotropic velocity checkerboard input model, **b** anisotropic input model of anomaly size 0.21° by 0.21° and fast polarization axes that are oriented perpendicular to each other (north and east), **c** and **e** are the recovered isotropic velocity models at 3.2 and 5.8 km depth slices, respectively. The color bar (in percent) represents the isotropic velocity perturbation with respect to the reference velocity model, **d** and **f** show the recovered models at 3.2 and 5.8 km depth levels, respectively, recovered from inversion of the input anisotropy model in **b**
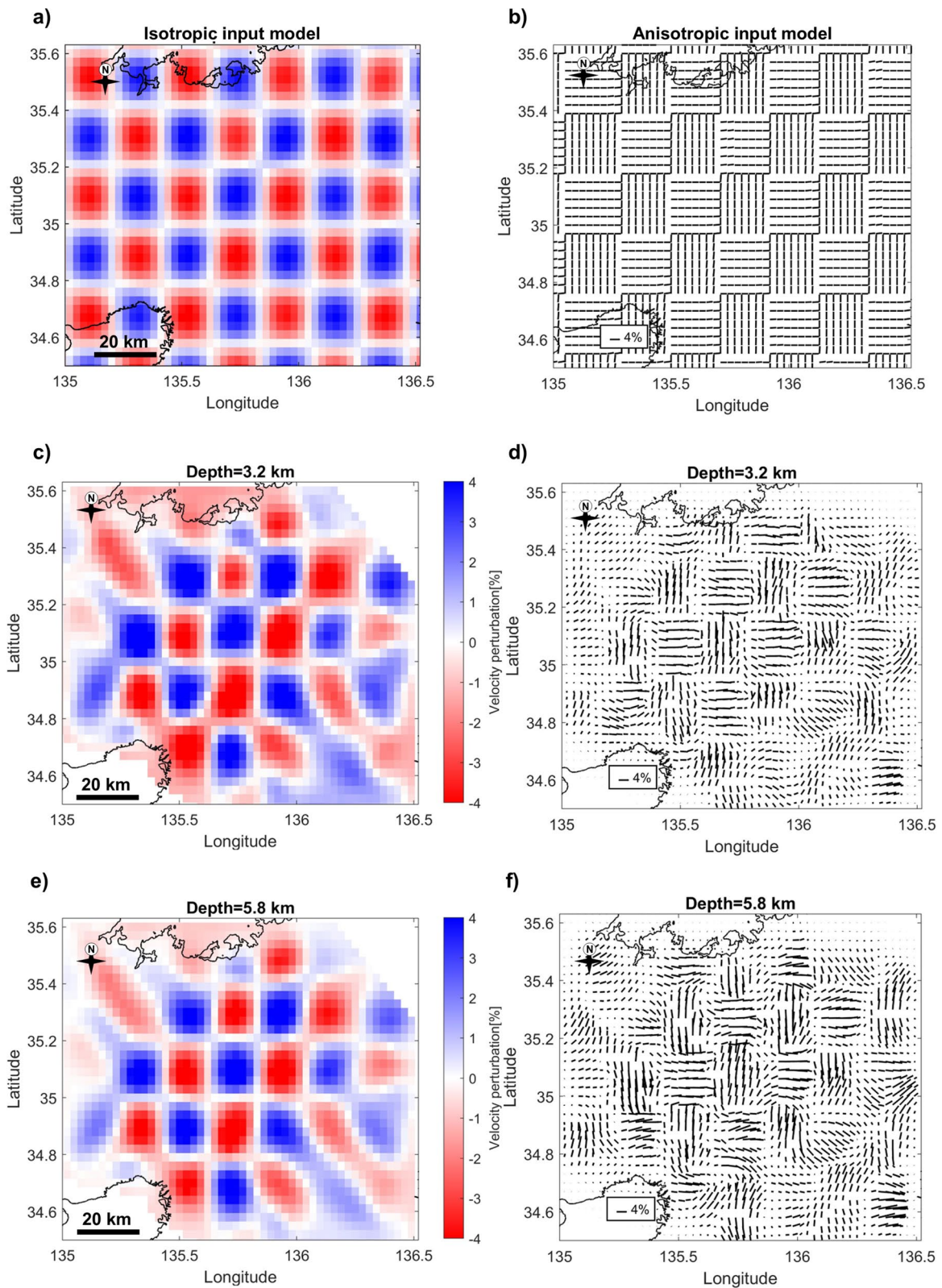
Nthaba *et al. Earth, Planets and Space* (2023) 75:102

Page 10 of 21
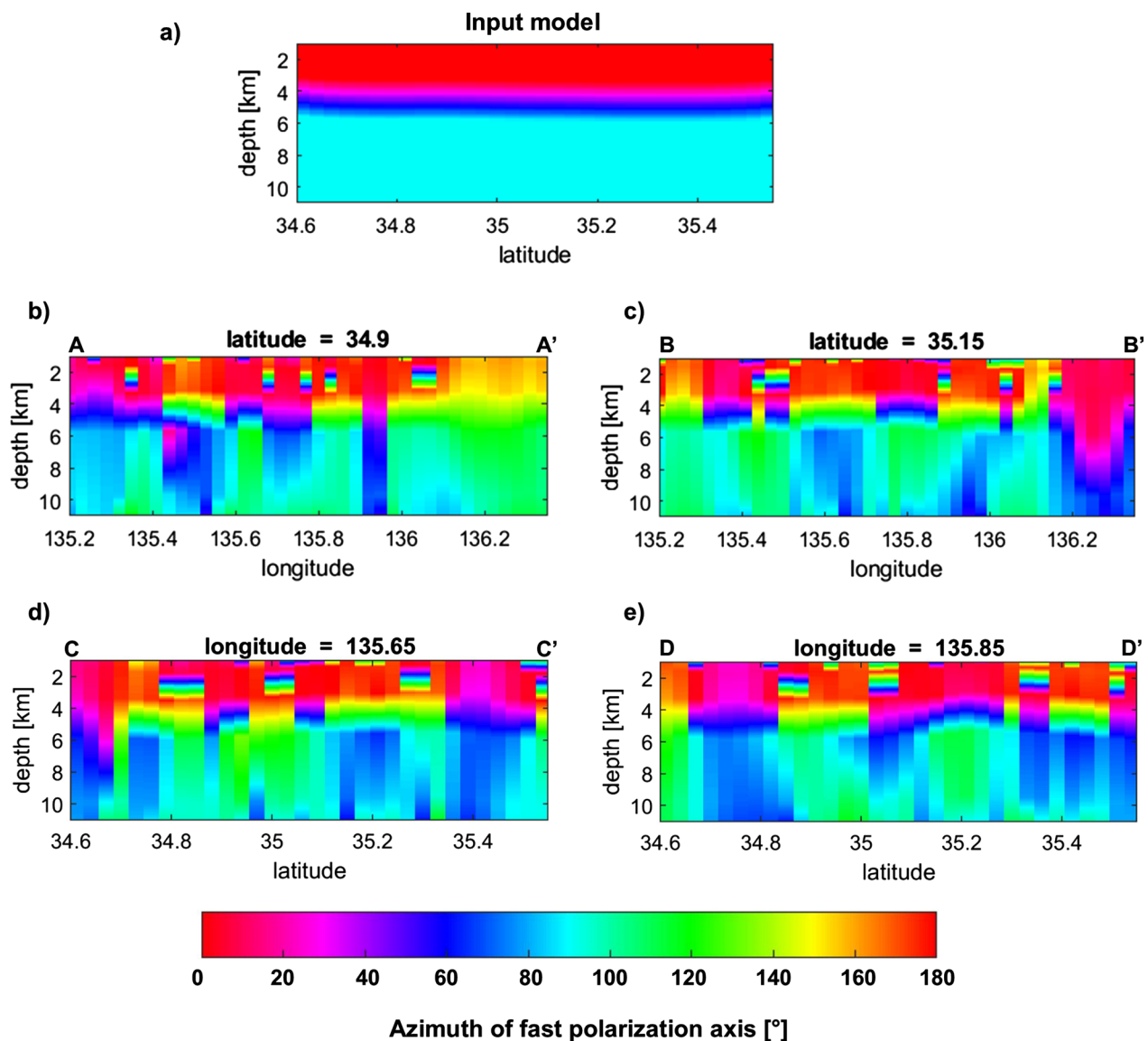

Fig. 4 (See legend on previous page.)

Fig. 5 The vertical resolution model for the central part of the study: **a** is the input anisotropic model and, **b–e** are the recovered anisotropic model from the inversion, showing the change in fast axis direction with depth

For example, tropical storms (i.e., dominant noise) can cause up to ~4% phase velocity perturbation (Weaver et al. 2009; Liu et al. 2019b), leading to errors in the estimated anisotropy. The frequency range of the ambient noise that we used in this study is 0.09–1.0 Hz, and the noise mainly originates from the ocean. Polarization analyses performed for the network used here (Additional file 1: Figure S1) show that an important contribution of noise sources observed in our study area emanates from the northwestern and southeastern parts of the study area, and are probably waves from the Japan Sea and the Pacific Ocean, respectively (Takagi et al. 2018). If the ocean is a strong noise source and affects our estimated

anisotropy, the estimated anisotropy could be parallel to the coastline. However, the direction of our estimated anisotropy varies significantly and is not consistent with the direction of the coastline. Therefore, we believe that our estimated anisotropy reflects crustal features such as stress orientation, although we cannot rule out the influence of the ambient noise propagation direction.

Interpretation

We compare azimuthal anisotropy results with the shear-wave splitting measurements (Hiramatsu et al. 1998; Hiramatsu et al. 2010; Iidaka et al. 2009; Iidaka et al. 2016; Kaneshima 1990), compressional stress trajectories
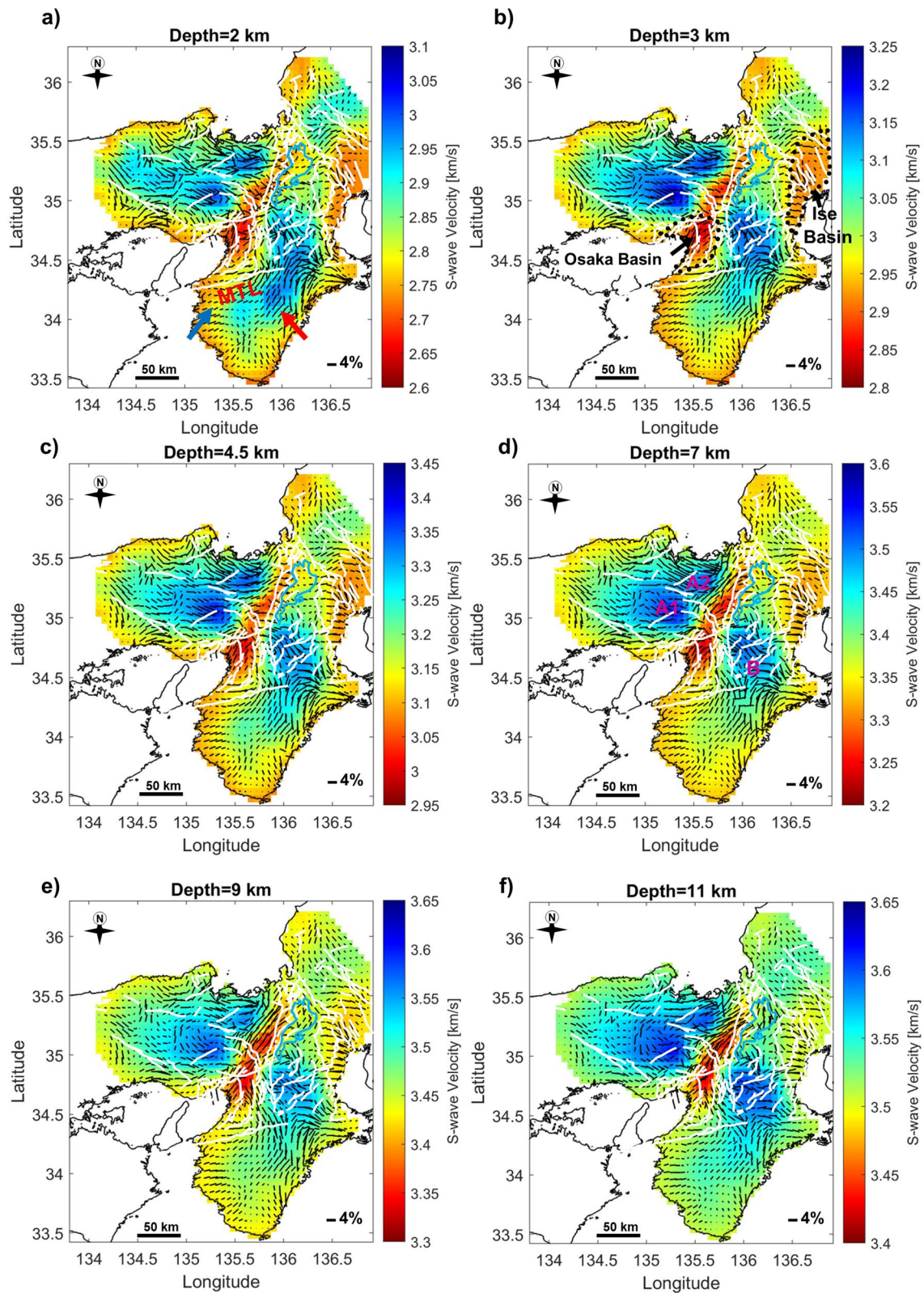
Fig. 6 **a**–**f** Horizontal slices showing the variation of isotropic S-wave velocities (background color) and azimuthal anisotropy (black bars) at discrete depth levels below sea level. White lines show the location of documented active faults. Depth (in km) is shown above each respective panel. Also shown is the location of the Median Tectonic Line (MTL) and sedimentary basins (black, dashed closed curves in **b**)
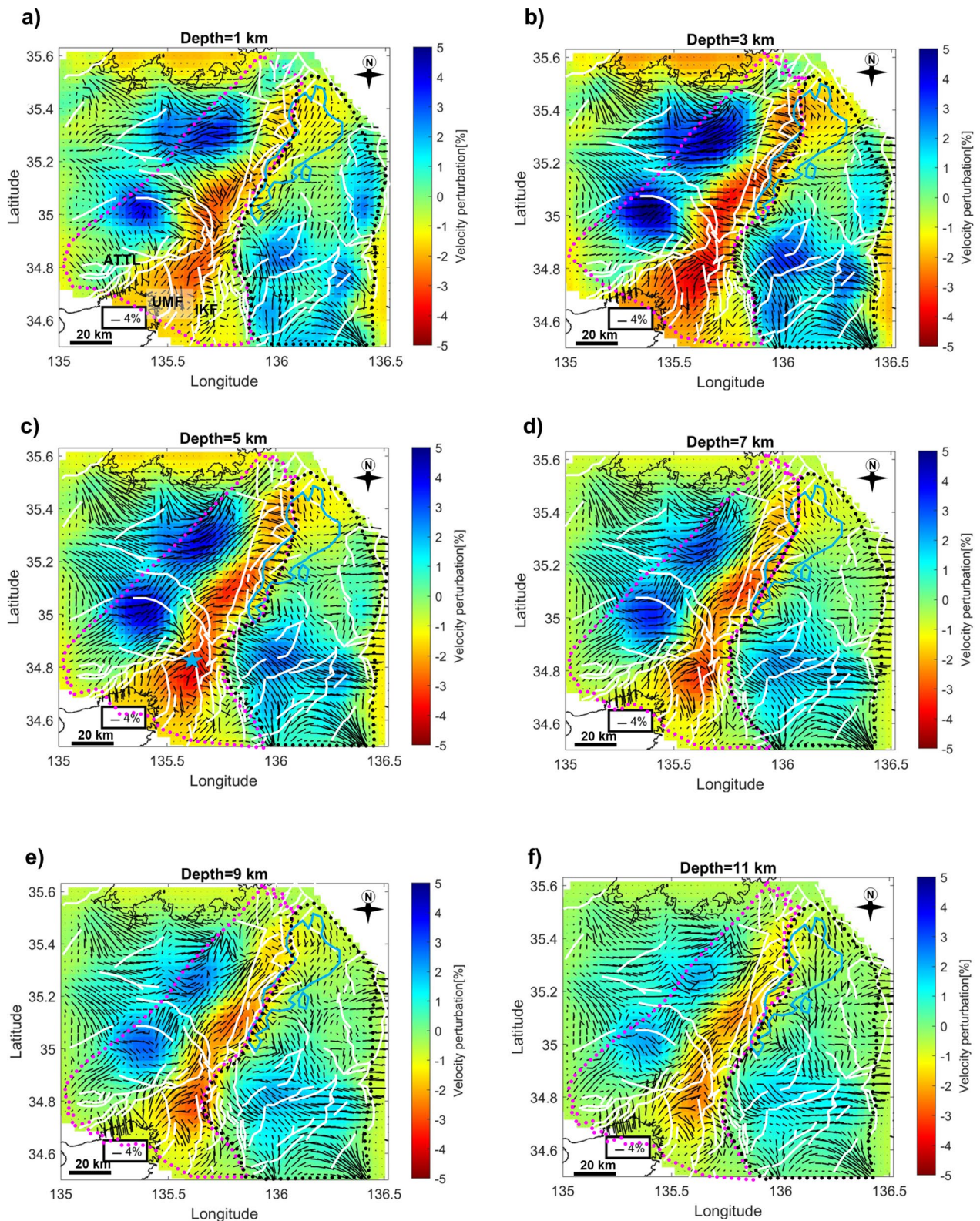
Fig. 7 **a–f** Horizontal slices showing the variation of isotropic S-wave velocities (background color) and azimuthal anisotropy (black bars) in the northern part of the Kinki region at discrete depth levels. Solid white lines indicate the location of documented active faults. Blue star in **c** represents the location of the 2018 Osaka earthquake. Dashed magenta and black closed curves represent two zones with contrasting anisotropy patterns. Depth (in km) is shown above each respective panel
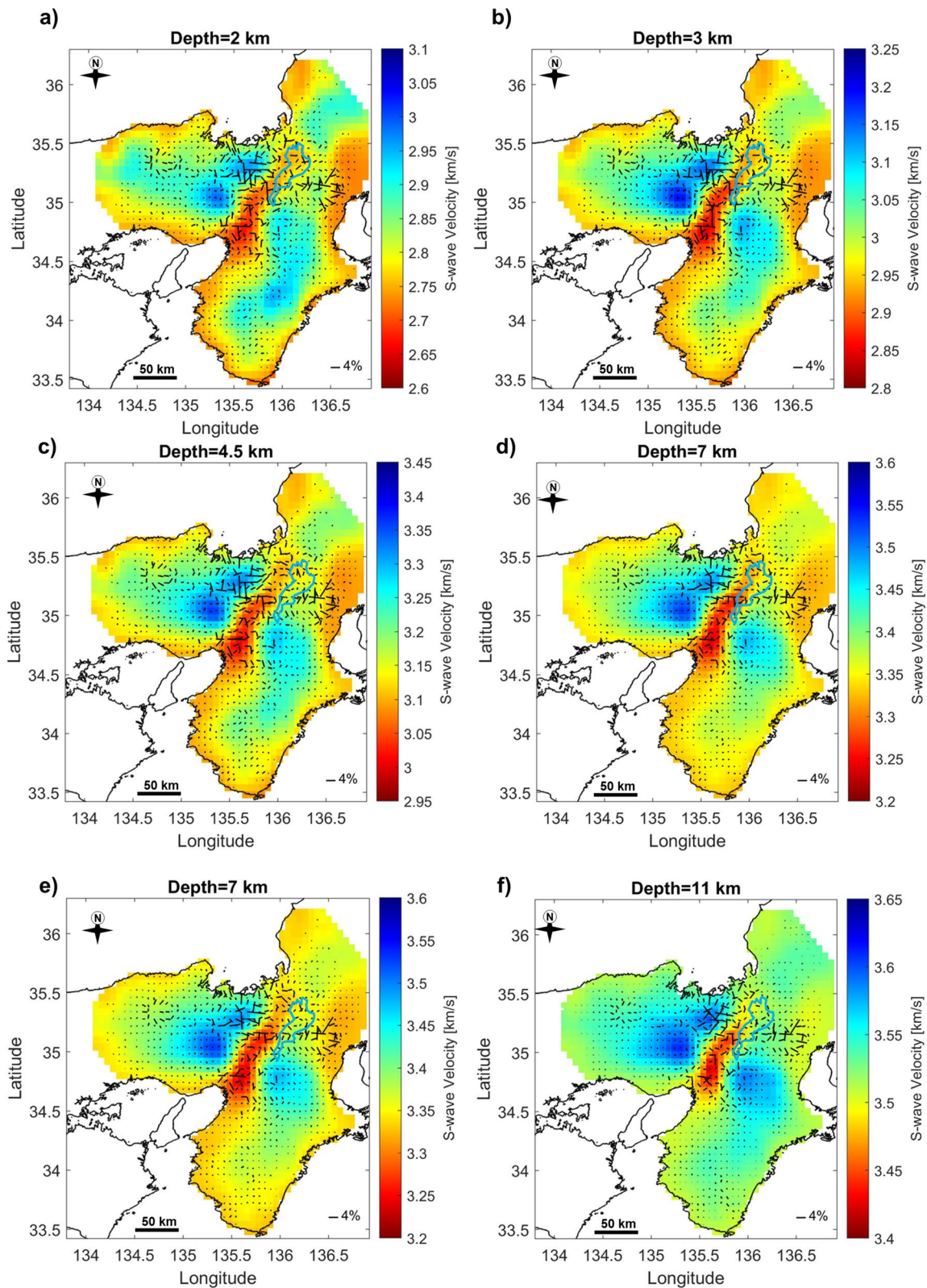
Fig. 8 a–f The anisotropy recovery test based on the isotropic S-wave velocity model without anisotropy (background color in Fig. 6) at discrete depth levels. Since the model has no anisotropy (only spatial variation of S-wave velocity), we expect no anisotropy in this results. The minor magnitude of azimuthal anisotropy compared to the estimated anisotropy (bars in Fig. 6) demonstrates the effectiveness of the inversion method used for anisotropy analysis
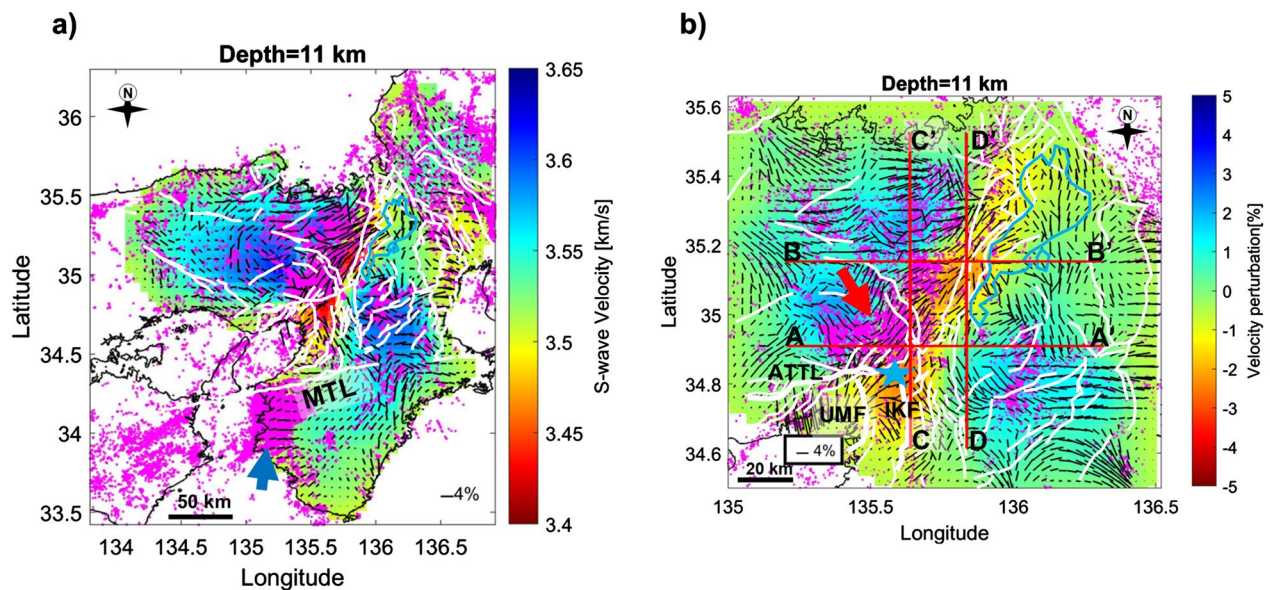
Nthaba *et al. Earth, Planets and Space*   (2023) 75:102

Page 15 of 21

Fig. 9 Horizontal slices showing the variation of isotropic S-wave velocities (background color) and azimuthal anisotropy (black bars) at 11 km depth. **a** Isotropic S-wave velocity and azimuthal anisotropy models of the entire Kinki region overlaid with earthquake hypocenters (magenta dots; Yano et al. 2017) and active faults. **b** Isotropic S-wave velocity and azimuthal anisotropy models of the northern part of the Kinki region overlaid with earthquake hypocenters (magenta dots; Yano et al. 2017) and active faults. Solid white lines show the location of documented active faults. Blue star in **b** indicates the location of the 2018 Osaka earthquake. Also shown are the locations of the Median Tectonic Line (MTL), Arima-Takatsuki Tectonic Line (ATTL), Uemachi Fault (UMF) and the Ikoma Fault (IKF)

(Ukawa 1982; Uchide et al. 2022) and the distribution the principal strain rate axes estimated from the continuous GPS velocity field (Sagiya et al. 2000). Additionally, we superimposed earthquake hypocenters occurring at a depth range of 4–11 km for the period 2001–2012 (Yano et al. 2017) on the isotropic velocity and anisotropic model (Fig. 9) in order to investigate the relationship between the seismic activity and the spatial distribution of anisotropy and isotropic velocity perturbations. Our results show a sharp contrast in the fast axes direction and anisotropy patterns between the northern (Inner Zone) and southern (Outer Zone) parts of the Kinki region. Potential sources of azimuthal anisotropy in each area are discussed below.

The southern part (Outer Zone) of the Kinki region
The Outer Zone exhibits coherent anisotropy with two prominent fast axes directions (i.e., E–W and NE–SW) (Fig. 6). The NE–SW fast-direction axes are persistent throughout the investigated depth range (2–11 km) and seem to be coast-parallel. This fast axes direction is consistent with both the trajectories of the maximum horizontal compressional stress (Uchide et al. 2022) and appear to be aligned in the same direction as the uplifted zone of the Kii Mountainland or normal to the ancient subduction direction (Fig. 1b; Tsuji et al. 2015). We posit that the anisotropy observed in the central part of the Kii

Mountainland could be largely influenced by the compressional stress field, or may be caused by the geological fabrics formed during the crustal shortening processes that yielded the mountain ranges in this area. According to Brocher and Christensen (1990), most of the rocks in the upper crust were formed at greater depths where temperatures and pressures induced anisotropy due to mineral alignment associated with foliation, and preserved this anisotropy when transported to the upper crust.

On the western side of the Kii Mountainland, prominent E–W fast axis direction is evident (Fig. 6). The fast axis direction is spatially coincident with both the low velocity anomaly in our isotropic velocity model and the dense distribution of earthquake hypocenters (dark blue arrow in Fig. 9a). Moreover, the fast axis direction is inconsistent with the NW–SE direction of the principal strain rate axes. However, the anisotropy orientation correlates well with both the compression stress trajectories (Ukawa 1982) and the orientation of the MTL, suggesting that the observed anisotropy in this area could either be stress-induced or structure-induced. In the latter case, we postulate that the strike-slip faulting of the MTL and its associated reactivation processes, or the mechanisms responsible for the seismic cluster prevailing here, may be having a strong influence on the observed azimuthal anisotropy in the western side of the Kii Mountainland,

Nthaba *et al. Earth, Planets and Space* (2023) 75:102

Page 16 of 21

or may be influenced by the geological formations in this area.

The northern part (Inner Zone) of the Kinki region

The fast axes polarizations show significant lateral and vertical variations in the Inner Zone of the Kinki region, revealing different patterns of azimuthal anisotropy. These anisotropy patterns and the fast axes directions can be observed clearly in the enlarged view of the central part of the Kinki region (Fig. 7). In Fig. 7, we identify three zones with interesting anisotropy patterns: the northwestern area (undemarcated zone in Fig. 7), the north central area (a zone demarcated by dashed, magenta closed curves in Fig. 7b–f), and northeastern part (dashed, black closed curves in Fig. 7a–f).

Northwestern part of the Kinki region

On the northwestern part of the Kinki region (undemarcated zone in Fig. 7), the fast polarization axes are oriented roughly E–W or WNW–ESE within the high velocity zone, and appear to have rotated clockwise to the NW–SE direction towards the northwestern edge of the

area. A few NE–SW-trending fast axes are also evident. In this area, prominent WNW–ESE fast axes directions are consistent throughout the investigated depth range of 1–11 km, and correlate well with the axis of maximum horizontal compression stress (Ukawa 1982) and the axis of maximum horizontal compression strain rate (Sagiya et al. 2000), suggesting that the sources of anisotropy are mainly from both the stress field and strain rate. Also, a rotation of the fast axis direction from roughly WNW–ESE to NW–SE proximal to the Japan sea coast may be indicating the existence of different deformation patterns resulting from stress changes towards the coast. Several studies have demonstrated that anisotropy observed in the upper crustal structure is associated primarily with the structural fabric and stress-induced microcracks alignment, with the fast axes directions aligning with these microcracks (Bem et al. 2022; Crampin 1978; Crampin and Peacock 2008; Yang et al. 2018).

Central part of the Kinki region

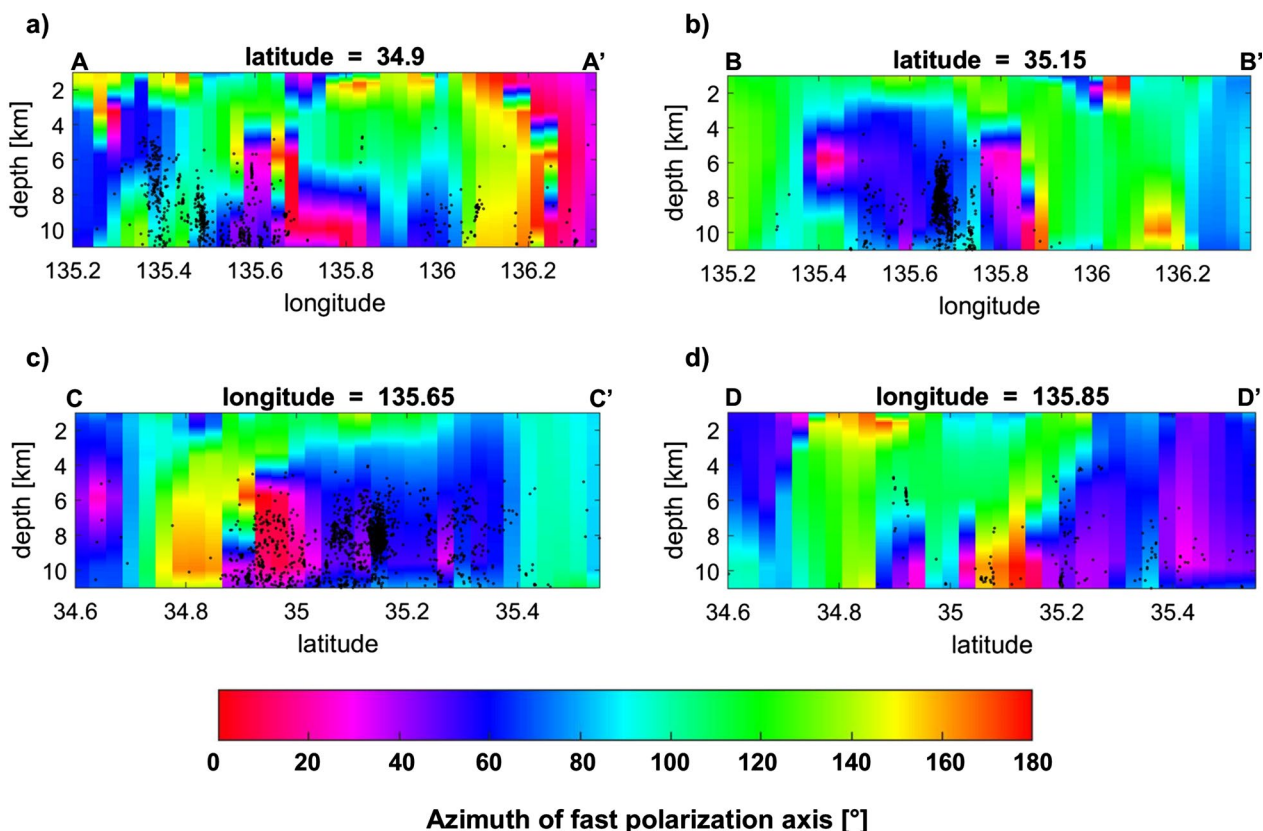On the central part of the Kinki region (a zone demarcated by dashed, magenta closed curves in Fig. 7), there is

Fig. 10 **a**–**d** Vertical slices of the profiles marked as red lines in Fig. 9b, showing the variation of fast axes direction with depth. Black dots indicate earthquake hypocenters ranging from 0 to 6.5 in moment magnitude for depths ranging 4–12 km (Yano et al. 2017). Background color represents azimuth of fast polarization axis
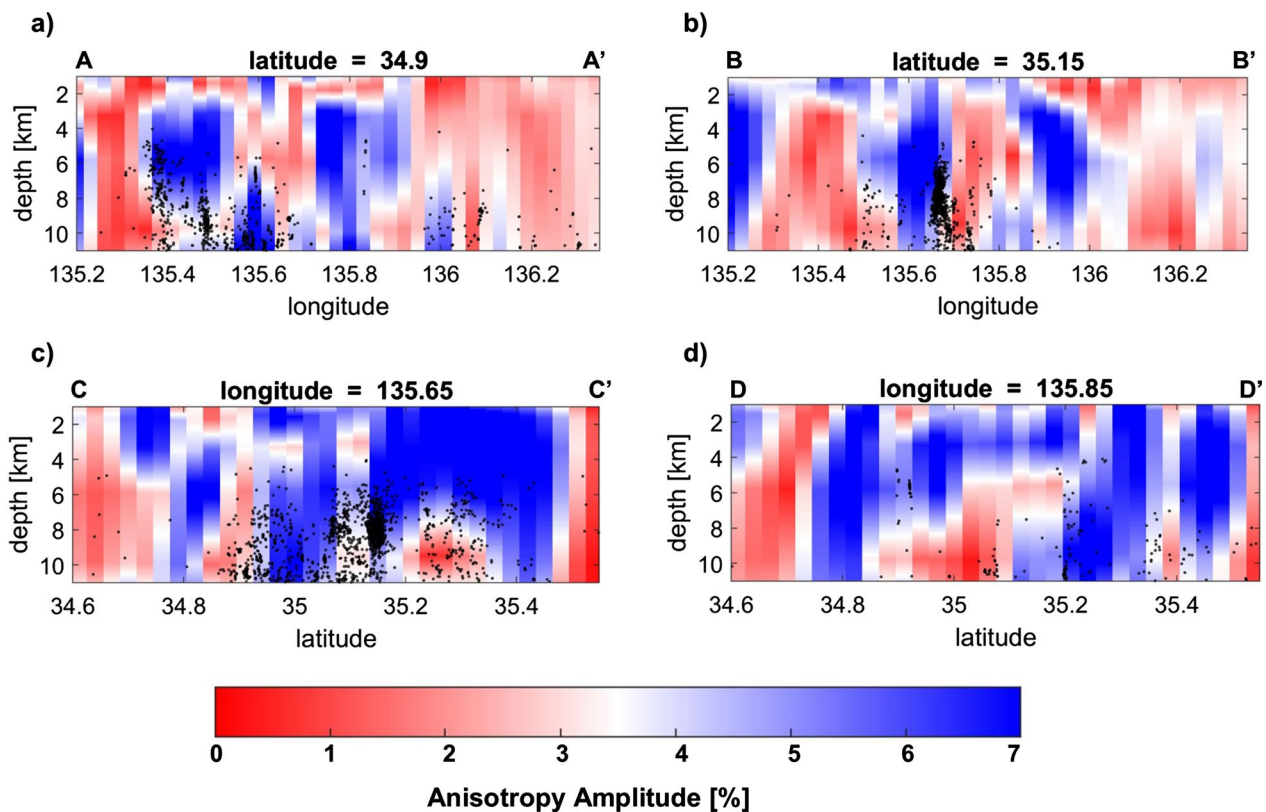
Nthaba *et al. Earth, Planets and Space* (2023) 75:102

Page 17 of 21

Fig. 11 a–d Vertical slices of the profiles marked as red lines in Fig. 9b, showing the variation of anisotropy amplitude both laterally and with depth. Black dots indicate earthquake hypocenters ranging from 0 to 6.5 in moment magnitude for depths ranging 4–12 km (Yano et al. 2017). Background color represents anisotropy amplitude

evident depth-dependent variation of the fast axes directions, changing from NW–SE and E–W (less than 3 km depth) to NE–SW (beneath 3 km depth). This change in the directions of the fast axes may be reflecting the existence of different deformational mechanisms in the upper crustal structure (less than 3 km depth) from the deeper parts (beneath 3 km depth). In this area, the axis of maximum horizontal compression stress and strain rate do not correlate well. The principal strain rate axes are oriented roughly WNW–ESE, while the axis of maximum horizontal compression stress are oriented roughly E–W. In the shallow part (less than 3 km depth), the observed anisotropy appears to be largely consistent with the principal strain rate axes (Sagiya et al. 2000). However, there are exceptions in some parts, for example, between latitudes 35.2–35.4 and longitudes 135.2–135.8 (high velocity zone in Fig. 7), where the near E–W oriented fast axes are significantly consistent with the directions of compressional stress trajectories (Ukawa 1982) than with the strain rate. Despite the poor correlation between strain rate and stress in this area, it is likely that the observed anisotropy in the shallower part (less than 3 km depth) may be stress-induced (Tsuji et al. 2011b). Beneath 3 km

depth, the fast axis direction (NE–SW) is consistent with the direction of the horizontal displacement rate vectors (Sagiya et al. 2000) but inconsistent with the orientation of the maximum horizontal compressional stress and the principal strain rate axes. Additionally, this NE–SW fast axes direction coincides majorly with the NE–SW-oriented Niigata-Kobe Tectonic Zone (NKTZ) and the NNE–SSW-trending west-dipping faults, designated the Biwako-seigan Fault Zone (BSFZ). Furthermore, in the central part of our study area, many earthquake hypocenters are aligned in the NE–SW direction, fitting well with the NE–SW polarized fast axes (Fig. 9). Therefore, there could be anisotropy mechanism change between shallow softer formation (stress-induced) and deep harder formation (structure-induced anisotropy).

In the southeast end of this area (red arrow in Fig. 9b), that is, proximal to the location of the 2018 Osaka earthquake of Mw 5.6 (blue star in Fig. 9b) and at a zone where the ENE–WSW strike-slip Arima-Takatsuki Tectonic Line (ATTL) links up with the N–S trending Uemachi fault (UMF) and Ikoma fault (IKF; Figs. 7a and 9b), NE–SW- and NW–SE-trending fast axes are observed. Here, earthquake hypocenters are densely aligned in the same

Nthaba *et al. Earth, Planets and Space*   (2023) 75:102

Page 18 of 21

direction as both the NW–SE and NE–SW-trending fast axes.

To examine the anisotropy characteristics with the depth, we created depth profiles of anisotropy azimuth and amplitude (Figs. 10 and 11). Although it is difficult to interpret smaller-scale anisotropy anomalies as indicated by the results of the vertical resolution test (Fig. 5), we can discern larger-scale anisotropy features. There is a clear correlation of earthquake hypocenters with the NE–SW fast axes directions below a depth of 4 km (Figs. 10a-d), and the magnitude of anisotropy varies significantly in zones spatially correlating with or proximal to the location of earthquake hypocenters (Figs. 11a–d). Therefore, we posit that the observed azimuthal anisotropy beneath a depth of 3 km may be linked to the localized, high-strain-rate crustal deformation, extensive faulting and its associated fault fabrics, shearing in these fault zones or earthquake-related fractures/cracks that are oriented in the same direction as the fast axes. Regarding the likely existence of fluid-filled cracks/fractures, our interpretation follows that of Hiramatsu et al. (1998), who suggested that the cause of the observed anisotropy in the central part of the Kinki region is related to the heterogeneous structures created by fluid-filled cracks, and the interpretation of Nakajima and Matsuzawa (2017), who attributed the apparent low-velocity and high-attenuation anomaly in this area to the presence of aqueous fluids.

To probe further, we compare our azimuthal anisotropy results with the shear-wave splitting measurements conducted by Hiramatsu et al. (2010) and Iidaka et al. (2016) in and around the north central part of our study area, which corresponds to areas 3 and 4 in Figs. 5 and 7 of Hiramatsu et al. (2010) and regions C and D in Fig. 3c of Iidaka et al. (2016). The dataset used in Hiramatsu et al. (2010) had source depths restricted within 30 km, whereas Iidaka et al. (2016) used a dataset consisting of earthquakes deeper than 230 km. In Hiramatsu et al. (2010), the fast axes are oriented in the NW–SE direction in this area, correlating well with only the fast axes directions observed at shallow depths (less than 3 km) in our model, and the observed maximum time delay values are about 0.1 s, which are typical values of crustal anisotropy; whereas, regions C and D of Iidaka et al. (2016) show NE–SW and ENE–WSW fast axes directions. Most of the observed time delay values (>0.5 s) in Iidaka et al. (2016) are significantly larger than the suggested maximum possible time delay values of shear-wave splitting due to crustal anisotropy (<0.2 s) for Japan (Kaneshima 1990). Based on the aforementioned time delay values and the source depths for the earthquakes used in the shear-wave splitting measurements (Iidaka et al. 2016), it is difficult to compare with our estimated anisotropy.

Unlike the shear-wave splitting measurements of Hiramatsu et al. (2010), our results resolve the depth-dependent variation of anisotropy in this area (Figs. 10 and 11). We attribute the observed anisotropy in shallower layers (less than 3 km) to the stressing rate or strain rate, as suggested by Hiramatsu et al. (2010). However, despite the consistency of our results with those of Iidaka et al. (2016) for zones beneath 3 km, we posit that the cause of anisotropy within 3–11 km depth range is caused mainly by structural features prevailing beneath the central zone of the Kinki region. Even so, it must be noted that we do not dispute the suggestion by Iidaka et al. (2016) that the anisotropy observed in regions C and D of their paper could be caused by the alignment of olivine crystals in the mantle wedge, with the crystal alignment inferred to be resulting from mantle flow related to subduction of the Pacific plate, considering the source depths of earthquakes used in their study.

Northeastern part of the Kinki region

We discuss the possible source of anisotropy observed in the northeastern part (a zone demarcated by dashed, black closed curves in Fig. 7), which forms part of the Kinki Triangle (Fig. 1c). This area has been dominated by the E–W compressional stress field, leading to the existence of predominantly N–S-oriented reverse active faults and some NE–SW or NW–SE strike-slip faults (Research Group for Active Faults of Japan 1991). It is suggested that the E–W-trending reverse faults occurred earlier than the N–S-trending reverse faults in the Kinki region (Hallo et al. 2019), and some of the older E–W-trending faults have since switched from reverse to strike-slip regime due to the presently active movements in the Kinki Triangle (Huzita 1969). In the northern part of this area, converging NW–SE and NE–SW fast axes directions and some curvilinear anisotropy patterns may be related to the geological structures such as faults and folds as opposed to the prevailing ambient stress field. In the southern part (high velocity zone in Fig. 7), however, the dominant NW–SE fast axes direction is significantly consistent with the direction of the principal strain rate axes (Sagiya et al. 2000), suggesting that in this area the strain rate strongly influences the observed anisotropy.

Conclusions

For the first time in the Kinki region, this study investigated 3D distribution of azimuthal anisotropy in its upper crustal structure. From the 6-month-long ambient noise data recorded by densely distributed seismic stations, we constructed a high spatial resolution 3D azimuthal anisotropic model of the Kinki region to a depth of about 11 km by ambient noise tomography approach. Our model shows detailed spatial variation

of azimuthal anisotropy compared with the previous studies that estimated anisotropy in some parts of the Kinki region from shear-wave splitting measurements. From our results, the following major conclusions were made:

1. Anisotropy patterns resolved in our model vary significantly across the Kinki region, suggesting a possibility of multistage crustal deformation and multiple sources of anisotropy in the Kinki region.
2. The Outer Zone exhibits coherent NE–SW-trending fast axes in the center of the Kii Mountainland, which are likely to be induced by the stress field, or geological fabrics generated by the extension and crustal shortening processes that yielded the Kii Mountainland.
3. The E–W and ENE–WSW trending fast polarization axis observed in the western side of the Kii Mountainland appear to be largely influenced by the horizontal compressional stress field. However, the activity of the Median Tectonic Line may also have a role in the anisotropy observed in this area.
4. The NW–SE-trending fast axes observed on the northern side of the Median Tectonic Line and also in the northwestern part of the Inner Zone are consistent with the maximum horizontal compression strain rate, and are also in agreement with the shear-wave splitting results reported in previous studies. Therefore, the observed anisotropy in these areas is likely to be largely influenced by strain rate.
5. In the central part of the Inner Zone (in and around the Niigata-Kobe Tectonic Zone), depth-dependent variation of anisotropy is evident, where the fast axes direction change, suggesting a possible existence of different deformational mechanisms in this area. We posit that anisotropy observed shallower than 3 km in the central part of the Inner Zone may be stress induced, whereas, anisotropy observed below a depth of 3 km is likely to be caused by the localized, high-strain-rate crustal deformation, which may as well be associated with the dense distribution of earthquakes in this zone, shearing or earthquake-related fractures/cracks oriented in the same direction as the fast axes direction.
6. In the eastern part of the Inner Zone, the converging NW–SE and NE–SW fast axes directions and some curvilinear anisotropy patterns may be related to the prevalent NE–SW or NW–SE strike-slip faults and folds in the Kinki Triangle (structure-induced anisotropy).

Abbreviations
AIST	National Institute of Advanced Industrial Science and Technology
ANT	Ambient noise tomography
ATTL	Arima-Takatsuki Tectonic Line
EUR	Eurasian
IKF	Ikoma Fault Zone
JMA	Japan Meteorological Agency
MTL	Median Tectonic Line
NIED	National Research Institute for Earth Science and Disaster Resilience
NKTZ	Niigata-Kobe Tectonic Zone
PHS	Philipine Sea
UMF	Uemachi Fault

Supplementary Information
The online version contains supplementary material available at https://doi.org/10.1186/s40623-023-01855-y.

> **Additional file 1: Figure S1.** The noise source direction for our dataset estimated from beamforming analysis.

Availability of data and materials
Continuous seismic waveform data from the Hi-net stations can be obtained from the NIED website (http://www.bosai.go.jp/e/). Continuous seismic data from the Kyushu University station, Tokyo University station, Nagoya University stations, AIST stations, Kyoto University stations, JMA stations and Kyoto University Manten project stations are available on request. The dispersion data used to produce Fig. 3c can be accessed at (https://doi.org/10.6084/m9.figshare.17989979). Our 3D azimuthal anisotropy of S-waves data is available from this URL (https://doi.org/10.6084/m9.figshare.21205262, Licence CC BY 4.0). Earthquake hypocenters used superimposed on our S-wave velocity models was published by the Japan Unified hI-resolution relocated Catalog for Earthquakes (JUICE) project, and can be accessed at this website (https://www.hinet.bosai.go.jp/topics/JUICE/3d/Juice_Hypo3D_Kinki_2001-2012.html; Yano et al. 2017).

Nthaba *et al. Earth, Planets and Space*   (2023) 75:102

Page 20 of 21

Declaration

Competing interests

Author details

[1]Department of Earth Resources Engineering, Kyushu University, 744 Motooka, Nishi-Ku, Fukuoka 819-0395, Japan. [2]Earth and Environmental Sciences Department, Botswana International University of Science and Technology, P/Bag 16, Palapye, Botswana. [3]International Institute for Carbon-Neutral Energy Research (WPI-I2CNER), Kyushu University, 744 Motooka, Nishi-Ku, Fukuoka 819-0395, Japan. [4]School of Engineering, The University of Tokyo, 7-3-1 Hongo, Bunkyo-Ku, Tokyo 113-8656, Japan. [5]Disaster Prevention Research Institute, Kyoto University, Kyoto, Japan.

References

Adimah NI, Padhy S (2020) Depth dependent azimuthal anisotropy in Madagascar island from ambient noise tomography. Tectonophysics 789:228513. https://doi.org/10.1016/j.tecto.2020.228513

Aki K (1957) Space and time spectra of stationary stochastic waves, with special reference to microtremors. Bull Earth Res Ins 35:415–456

Ando M (1979) The stress field of the Japanese Island in the last 0.5 million years. In Earth Mon. Symp 7:541–546

Balfour NJ, Savage MK, Townend J (2005) Stress and crustal anisotropy in Marlborough, New Zealand: evidence for low fault strength and structure-controlled anisotropy. Geophys J Int 163(3):1073–1086. https://doi.org/10.1111/j.1365-246X.2005.02783.x

Barnes GL (2008) The making of the Japan Sea and the Japanese mountains: understanding Japan's volcanism in structural context. Jpn Rev 20:3–52

Bem TS, Liu C, Yao H et al (2022) Azimuthally anisotropic structure in the crust and uppermost mantle in central east China and its significance to regional deformation around the Tan-Lu Fault zone. J Geophys Res Solid Earth 127:e2021JB023532. https://doi.org/10.1029/2021JB023532

Boness NL, Zoback MD (2006) Mapping stress and structurally controlled crustal shear velocity anisotropy in California. Geology 34:825–828. https://doi.org/10.1130/G22309.1

Brocher TM, Christensen NI (1990) Seismic anisotropy due to preferred mineral orientation observed in shallow crustal rocks in southern Alaska. Geology 18:737–740. https://doi.org/10.1130/0091-7613(1990)018%3C0737:SADTPM%3E2.3.CO;2

Chang LJ, Ding ZF, Wang CY (2015) Upper mantle anisotropy beneath the southern segment of North-South tectonic belt, China. Chin J Geophys 58:4052–4067. https://doi.org/10.6038/cjg20151114

Chen D, Zhang F, Chen H et al (2015) Structural architecture and tectonic evolution of the Fangzheng sedimentary basin (NE China), and implications for the kinematics of the Tan-Lu fault zone. J Asian Earth Sci 106:34–48. https://doi.org/10.1016/j.jseaes.2015.02.028

Chen KX, Gung Y, Kuo BY et al (2018) Crustal magmatism and deformation fabrics in northeast Japan revealed by ambient noise tomography. J Geophys Res Solid Earth 123:8891–8906. https://doi.org/10.1029/2017JB015209

Choi PY, Nakae S, Kim H (2011) Fault tectonic analysis of Kii peninsula, Southwest Japan: preliminary approach to Neogene paleostress sequence near the Nankai subduction zone. Isl 20:455–476. https://doi.org/10.1111/j.1440-1738.2011.00779.x

Crampin S (1977) A review of the effects of anisotropic layering on the propagation of seismic waves. Geophys J Int 49:9–27. https://doi.org/10.1111/j.1365-246X.1977.tb03698.x

Crampin S (1978) Seismic-wave propagation through a cracked solid: polarization as a possible dilatancy diagnostic. Geophys J Int 53:467–496. https://doi.org/10.1111/j.1365-246X.1978.tb03754.x

Crampin S (1998) Shear-wave splitting in a critical crust: the next step. Rev Inst Fr Pét 53:749–763

Crampin S, Peacock S (2008) A review of the current understanding of seismic shear-wave splitting in the Earth's crust and common fallacies in interpretation. Wave Motion 45:675–722. https://doi.org/10.1016/j.wavemoti.2008.01.003

Ekström G (2014) Love and Rayleigh phase-velocity maps, 5–40 s, of the western and central USA from USArray data. Earth Planet Sci Lett 402:42–49. https://doi.org/10.1016/j.epsl.2013.11.022

Ekström G, Abers GA, Webb SC (2009) Determination of surface-wave phase velocities across USArray from noise and Aki's spectral formulation. Geophys Res Lett 36:5–9. https://doi.org/10.1029/2009GL039131

Fang H, Yao H, Zhang H et al (2015) Direct inversion of surface wave dispersion for three-dimensional shallow crustal structure based on ray tracing: methodology and application. Geophys J Int 201:1251–1263. https://doi.org/10.1093/gji/ggv080

Guo Z, Chen YJ (2017) Mountain building at northeastern boundary of Tibetan Plateau and craton reworking at Ordos block from joint inversion of ambient noise tomography and receiver functions. Earth Planet Sci Lett 463:232–242. https://doi.org/10.1016/j.epsl.2017.01.026

Hallo M, Opršal I, Asano K et al (2019) Seismotectonics of the 2018 northern Osaka M6.1 earthquake and its aftershocks: joint movements on strike-slip and reverse faults in inland Japan. Earth Planet Space 71:1–21. https://doi.org/10.1186/s40623-019-1016-8

Hiramatsu Y, Ando M, Tsukuda T et al (1998) Three-dimensional image of the anisotropic bodies beneath central Honshu, Japan. Geophys J Int 135:801–816. https://doi.org/10.1046/j.1365-246X.1998.00663.x

Hiramatsu Y, Iwatsuki K, Ueyama S et al (2010) Spatial variation in shear wave splitting of the upper crust in the zone of inland high strain rate, central Japan. Earth Planet Space 62:675–684. https://doi.org/10.5047/eps.2010.08.003

Huzita K (1969) Tectonic development of southwest Japan in the Quaternary period. J Geosci Osaka City Univ 12:53–70

Huzita K (1980) Role of the Median Tectonic Line in the Quaternary tectonics of the Japanese Islands. Mem Geol Soc Japan 18:129–153

Iidaka T, Hiramatsu Y, The Japanese University Group of the Joint Seismic Observations at NKTZ (2009) Shear-wave splitting analysis of the upper mantle at the Niigata-Kobe Tectonic Zone with the data of the Joint Seismic Observations at NKTZ. Earth Planet Space. 61:227–235. https://doi.org/10.1186/BF03352903

Iidaka T, Hiramatsu Y, The Research Group for the Joint Seismic Observations at the Nobi Area (2016) Heterogeneous mantle anisotropy and fluid upwelling: implication for generation of the 1891 Nobi earthquake. Earth Planet Space. 68:1–9. https://doi.org/10.1186/s40623-016-0540-z

Iio Y, Kishimoto S, Nakao S et al (2018) Extremely weak fault planes: an estimate of focal mechanisms from stationary seismic activity in the San'in district, Japan. Tectonophysics 723:136–148. https://doi.org/10.1016/j.tecto.2017.12.007

Kaneshima S (1990) Origin of crustal anisotropy: Shear wave splitting studies in Japan. J Geophys Res Solid Earth 95:11121–11133. https://doi.org/10.1029/JB095iB07p11121

Kaneshima S, Ando M, Crampin S (1987) Shear-wave splitting above small earthquakes in the Kinki district of Japan. Phys Earth Planet Inter 45:45–58. https://doi.org/10.1016/0031-9201(87)90196-8

Katoh S, Iio Y, Katao H et al (2018) The relationship between S-wave reflectors and deep low-frequency earthquakes in the northern Kinki district, southwestern Japan. Earth Planets Space 70:1–11. https://doi.org/10.1186/s40623-018-0921-6

Legendre CP, Zhao L, Tseng TL (2021) Large-scale variation in seismic anisotropy in the crust and upper mantle beneath Anatolia, Turkey. Commun Earth Environ 2:1–7. https://doi.org/10.1038/s43247-021-00142-6

Li C, Yao H, Fang H et al (2016) 3D near-surface shear-wave velocity structure from ambient-noise tomography and borehole data in the Hefei urban area, China. Seismol Res Lett 87:882–892. https://doi.org/10.1785/0220150257

Li T, Gu YJ, Wang Z et al (2019) Spatiotemporal variations in crustal seismic anisotropy surrounding induced earthquakes near Fox Creek, Alberta. Geophys Res Lett 46:5180–5189. https://doi.org/10.1029/2018GL081766

Liu C, Yao H, Yang HY et al (2019a) Direct inversion for three-dimensional shear wave speed azimuthal anisotropy based on surface wave ray tracing: Methodology and application to Yunnan, southwest China. J Geophys Res Solid Earth 124:11394–11413. https://doi.org/10.1029/2018JB016920

Liu X, Beroza GC, Nakata N (2019b) Isolating and suppressing the spurious non-diffuse contributions to ambient seismic field correlations. J

Nthaba *et al. Earth, Planets and Space*   (2023) 75:102

Page 21 of 21

Geophys Res Solid Earth 124:9653–9663. https://doi.org/10.1029/2019J B017297

Matsubara M, Obara K, Kasahara K (2008) Three-dimensional P-and S-wave velocity structures beneath the Japan Islands obtained by high-density seismic stations by seismic tomography. Tectonophysics 454:86–103. https://doi.org/10.1016/j.tecto.2008.04.016

Mizuno T, Yomogida K, Ito H (2001) Spatial distribution of shear wave anisotropy in the crust of the southern Hyogo region by borehole observations. Geophys J Int 147:528–542. https://doi.org/10.1046/j.1365-246x.2001. 01534.x

Montagner JP, Nataf HC (1986) A simple method for inverting the azimuthal anisotropy of surface waves. J Geophys Res Solid Earth 91:511–520. https://doi.org/10.1029/JB091iB01p00511

Montagner JP, Tanimoto T (1991) Global upper mantle tomography of seismic velocities and anisotropies. J Geophys Res Solid Earth 96:20337–20351. https://doi.org/10.1029/91JB01890

Nakajima J, Hasegawa A (2007) Subduction of the Philippine Sea plate beneath southwestern Japan: Slab geometry and its relationship to arc magmatism. J Geophys Res Solid Earth. https://doi.org/10.1029/2006J B004770

Nakajima J, Matsuzawa T (2017) Anelastic properties beneath the Niigata-Kobe tectonic zone, Japan. Earth Planet Space 69:1–9. https://doi.org/10.1186/ s40623-017-0619-1

Nakata T, Imaizumi T (2002) Digital active fault map of Japan. University of Tokyo press, Tokyo (**in Japanese**)

Nishida K, Kawakatsu H, Obara K (2008) Three-dimensional crustal S wave velocity structure in Japan using microseismic data recorded by Hi-net tiltmeters. J Geophys Res Solid Earth. https://doi.org/10.1029/2007JB0053 95

Nthaba B, Ikeda T, Nimiya H et al (2022) (2022) Ambient noise tomography for a high-resolution 3D S-wave velocity model of the Kinki Region, Southwestern Japan, using dense seismic array data. Earth Planet Space 74:96. https://doi.org/10.1186/s40623-022-01654-x

Ojo AO, Ni S, Chen H et al (2018) Crust-mantle coupling mechanism in Cameroon, West Africa, revealed by 3D S-wave velocity and azimuthal anisotropy. Phys Earth Planet Inter 274:195–213. https://doi.org/10.1016/j. pepi.2017.12.006

Okamura Y, Shishikura M (2020) New hypothesis to explain Quaternary forearc deformation and the variety of plate boundary earthquakes along the Suruga-Nankai Trough by oblique subduction of undulations on the Philippine Sea Plate. Earth Planet Space 72:1–14. https://doi.org/10.1186/ s40623-020-01183-5

Paige CC, Saunders MA (1982) LSQR: An algorithm for sparse linear equations and sparse least squares. ACM Trans Math Softw 8:43–71. https://doi.org/ 10.1145/355984.355989

Rawlinson N, Sambridge M (2004) Wave front evolution in strongly heterogeneous layered media using the fast marching method. Geophys J Int 156:631–647. https://doi.org/10.1111/j.1365-246X.2004.02153.x

Research Group for Active Faults of Japan (1991) Active faults in Japan: Sheet maps and inventories. University of Tokyo press, Tokyo, p 437

Sadeghisorkhani H, Gudmundsson Ó, Tryggvason A (2018) GSpecDisp: a matlab GUI package for phase-velocity dispersion measurements from ambient-noise correlations. Comput Geosci 110:41–53. https://doi.org/ 10.1016/j.cageo.2017.09.006

Sagiya T, Miyazaki SI, Tada T (2000) Continuous GPS array and present-day crustal deformation of Japan. Pure Appl Geophys 157:2303–2322. https:// doi.org/10.1007/PL00022507

Sato H, Kato N, Abe S et al (2015) Reactivation of an old plate interface as a strike-slip fault in a slip-partitioned system: Median tectonic line, SW Japan. Tectonophysics 644:58–67. https://doi.org/10.1016/j.tecto.2014. 12.020

Savage MK (1999) Seismic anisotropy and mantle deformation: what have we learned from shear wave splitting? Rev Geophys 37:65–106. https://doi. org/10.1029/98RG02075

Smith ML, Dahlen FA (1973) The azimuthal dependence of Love and Rayleigh wave propagation in a slightly anisotropic medium. J Geophys Res 78:3321–3333. https://doi.org/10.1029/JB078i017p03321

Suemoto Y, Ikeda T, Tsuji T, Iio Y (2020) Identification of a nascent tectonic boundary in the San-in area, southwest Japan, using a 3D S-wave velocity structure obtained by ambient noise surface wave tomography. Earth Planet Space 72(1):1–13. https://doi.org/10.1186/s40623-020-1139-y

Sugiyama Y (1992) Neotectonics of the forearc zone and the Setouchi province in southwest Japan. Chishitsugaku Ronshū 40:219–233

Takagi R, Nishida K, Maeda T et al (2018) Ambient seismic noise wavefield in Japan characterized by polarization analysis of Hi-net records. Geophys J Int 182:461–476. https://doi.org/10.1093/gji/ggy334

Tamura T, Oohashi K, Otsubo M et al (2020) Contribution to crustal strain accumulation of minor faults: a case study across the Niigata-Kobe Tectonic Zone, Japan. Earth Planet Space 72:1–17. https://doi.org/10.1186/ s40623-020-1132-5

Teanby NA, Kendall JM, Van der Baan M (2004) Automation of shear-wave splitting measurements using cluster analysis. Bull Seismol Soc Am 94:453–463. https://doi.org/10.1785/0120030123

Tsuji T, Hino R, Sanada Y, Yamamoto K, Park JO, No T, Araki E, Bangs N, von Huene R, Moore G, Kinoshita M (2011a) In situ stress state from walka-round VSP anisotropy in the Kumano basin southeast of the Kii Peninsula, Japan. Geochem Geophys Geosyst 12(9):19. https://doi.org/10.1029/ 2011GC003583

Tsuji T, Dvorkin J, Mavko G et al (2011b) VP/VS ratio and shear-wave splitting in the Nankai Trough seismogenic zone: insights into effective stress, pore pressure, and sediment consolidation. Geophysics 76:WA71–WA82. https://doi.org/10.1190/1.3560018

Tsuji T, Ashi J, Strasser M et al (2015) Identification of the static backstop and its influence on the evolution of the accretionary prism in the Nankai Trough. Earth Planet Sci Lett 431:15–25. https://doi.org/10.1016/j.epsl. 2015.09.011

Uchide T, Shiina T, Imanishi K (2022) Stress map of Japan: detailed nationwide crustal stress field inferred from focal mechanism solutions of numerous microearthquakes. J Geophys Res Solid Earth. 127:e2022JB024036. https://doi.org/10.1029/2022JB024036

Ukawa M (1982) Lateral stretching of the Philippine Sea plate subducting along the Nankai-Suruga trough. Tectonics 1:543–571. https://doi.org/10. 1029/TC001i006p00543

Wang Z, Zhao D (2021) 3D anisotropic structure of the Japan subduction zone. Sci Adv 7:eabc9620. https://doi.org/10.1126/sciadv.abc9620

Wang M, Hubbard J, Plesch A et al (2016) Three-dimensional seismic velocity structure in the Sichuan basin, China. J Geophys Res Solid Earth 121:1007–1022. https://doi.org/10.1002/2015JB012644

Weaver R, Froment B, Campillo M (2009) On the correlation of non-isotropically distributed ballistic scalar diffuse waves. J Acoust Soc Am 126:1817–1826. https://doi.org/10.1121/1.3203359

Wu C, Xu T, Ai Y (2021) Crustal azimuthal anisotropy in the Jiaodong peninsula: evidence for the suture between the North China Craton and South China block. Phys Earth Planet Inter 314:106705. https://doi.org/10.1016/j. pepi.2021.106705

Xu X, Ding Z, Li L et al (2021) Crustal Anisotropy beneath the trans-north China orogen and its adjacent areas from receiver functions. Front Earth Sci. https://doi.org/10.3389/feart.2021.753612

Yang HY, Hung SH (2005) Validation of ray and wave theoretical travel times in heterogeneous random media. Geophys Res Lett. https://doi.org/10. 1029/2005GL023501

Yang Y, Yao H, Zhang P et al (2018) Crustal azimuthal anisotropy in the trans-North China orogen and adjacent regions from receiver functions. Sci China Earth Sci 61:903–913. https://doi.org/10.1007/s11430-017-9209-9

Yano TE, Takeda T, Matsubara M et al (2017) Japan unified high-resolution relocated catalog for earthquakes (JUICE): crustal seismicity beneath the Japanese Islands. Tectonophysics 702:19–28. https://doi.org/10.1016/j. tecto.2017.02.017

Yao H, Van Der Hilst RD, Montagner JP (2010) Heterogeneity and anisotropy of the lithosphere of SE Tibet from surface wave array tomography. J Geophys Res Solid Earth. https://doi.org/10.1029/2009JB007142

Publisher's Note